Journal Pre-proof

Vibration and damping study of multifunctional grille composite sandwich plates with an IMAS design approach

Hui Li, Xintong Wang, Xiaoyue Hu, Jian Xiong, Qingkai Han, Xiangping Wang, Zhongwei Guan

PII: S1359-8368(21)00462-5

DOI: https://doi.org/10.1016/j.compositesb.2021.109078

Reference: JCOMB 109078

To appear in: *Composites Part B*

Received Date: 2 February 2021

Revised Date: 9 June 2021

Accepted Date: 10 June 2021

Please cite this article as: Li H, Wang X, Hu X, Xiong J, Han Q, Wang X, Guan Z, Vibration and damping study of multifunctional grille composite sandwich plates with an IMAS design approach, *Composites Part B* (2021), doi: https://doi.org/10.1016/j.compositesb.2021.109078.

Author Statement

Hui Li: Conceptualization, Methodology, Writing- Original draft preparation

Xintong Wang: Formal analysis, Software, Programming

Xiaoyue Hu: Visualization, Programming

Jian Xiong: Investigation, Writing - Review & Editing, Supervision

Qingkai Han: Conceptualization, Methodology, Supervision

Xiangping Wang: Methodology, Validation

Zhongwei Guan: Investigation, Validation, Supervision

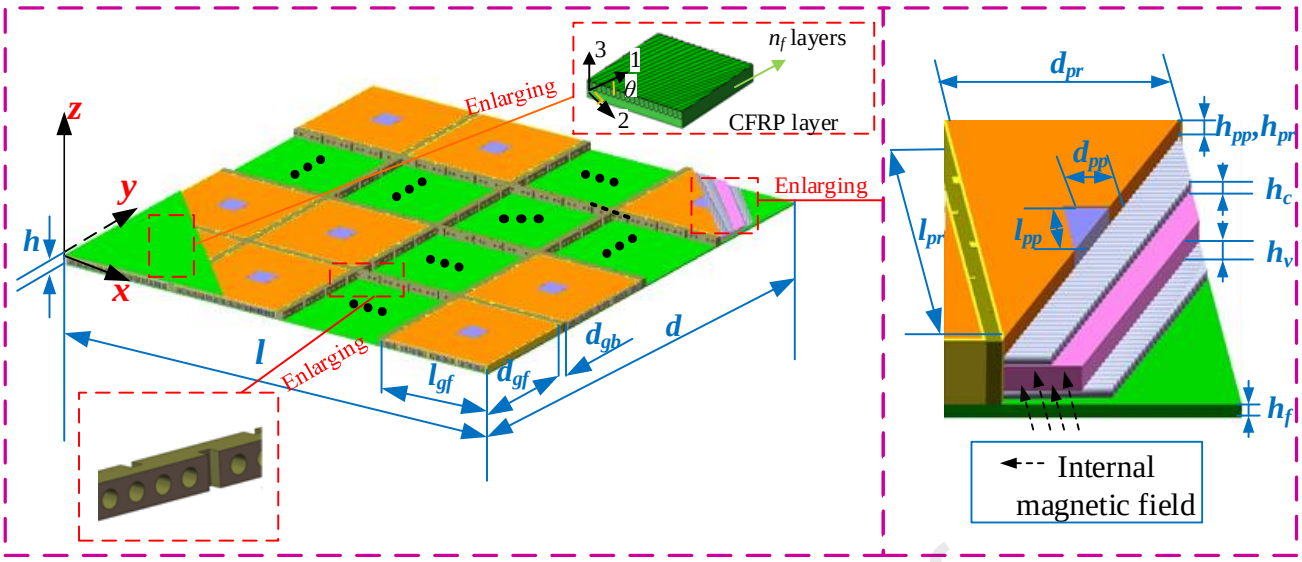

Fig 3. A dynamic model of the CFRP-GFB-GFU plate

Vibration and damping study of multifunctional grille composite sandwich plates with an IMAS design approach

*Hui Li[1,2,4,6], Xintong Wang[1,2], Xiaoyue Hu[1,2], Jian Xiong[*3], Qingkai Han[1], Xiangping Wang[4], Zhongwei Guan[5,6]*
1 School of Mechanical Engineering and Automation, Northeastern University, Shenyang, 110819, China
2 State Key Laboratory of High Performance Complex Manufacturing, Central South University, Changsha, 410083, China
3 Center for Composite Materials and Structures, Harbin Institute of Technology, Harbin 150001, China
4 Key Laboratory of Impact Dynamics on Aero Engine, Shenyang 110015, China
5 Advanced Materials Research Centre, Technology Innovation Institute, Masdar City, Abu Dhabi, UAE
6 School of Engineering, University of Liverpool, Brownlow Street, Liverpool L69 3GQ, United Kingdom

Abstract: In the present study, an integrated material and structure (IMAS) design approach is proposed for fabrication of a multifunctional grille composite sandwich plate. It consists of two panels made of carbon fiber/resin polymer (CFRP) and one grille functional core that includes several grid frame beams (GFBs) and grille functional units (GFUs) via falcon riveting connections to achieve vibration sensing and damping control functions. In each GFU, it is composed of a rectangular grille (RG) and several embedded functional materials with 4-layer laminates, including a piezoelectric sensing layer, an upper copper wire layer, a magnetorheological elastomer (MRE) layer and a lower copper wire layer. To investigate the free vibration and damping characteristics of such a highly integrated sandwich structure, an analytical model is proposed that is based on the complex modulus method, the polynomial expansion approach, the improved Rayleigh-Ritz method, etc. After the natural frequencies, modal shapes and damping parameters are successfully solved, with results from literature being employed to roughly validate the model developed. Meanwhile, the dynamic experiments with different internal magnetic field distribution patterns and intensities of MRE are undertaken to give a further validation of the present model. Finally, the parameter analysis is carried out and some important conclusions are summarized to better exert active and passive vibration suppression performance of the CFRP-GFB-GFU plate.

Keywords: A. integrated design approach; B. Vibration perception; C. Vibration control; D. Grille composite plate; E. internal magnetic field

[*] Corresponding author, Tel.: +86 451 86412549; E-mail address: jx@hit.edu.cn (Prof. Jian Xiong)

1. Introduction

Composite sandwich plates are extensively used as the key components in aerospace, marine and other engineering fields, due to their lightweight and excellent mechanical properties [1-5]. However, as they are often servicing in a harsh environment and extreme loading conditions [6-8], the excessive vibration [9-11], bending deformation [12-13] delamination [14], fatigue [15] and other severe problems [16-17] have increasingly become popular research topics.

In the past decades, a variety of damping methods have been adopted to study the vibration suppression issues of composite structures, which are generally categorized as three approaches, i.e. the passive damping method (PDM), active damping method (ADM) and integrated active and passive damping method (A&PDM). As those methods have their respective advantages and disadvantages, it is difficult to say which one is more practical or suitable for applications. With the deep utilization of PDM, Chen and Huang [18] studied the vibration suppression effect of a rectangular plate with constrained layer damping (CLD) treatment. Based on the modal strain energy method, Kumar and Singh [19] conducted the detailed finite element (FE) simulations on the damping property of a curved panel with different CLD patches and sticking locations. By adopting a differential transform method, Arikoglu and Ozkol [20] successfully obtained the free vibration solution of a sandwich composite beam with a viscoelastic core. Using the simplified-super-element-method, Zhou et al. [21] theoretically investigated the vibration suppression effect of a periodically stiffened-thin-plate embedded with the viscoelastic damping material. By adopting the improved Rayleigh-Ritz approach, Song et al. [22] studied the free vibration and damping behaviors of a thin short cylindrical shell with viscoelastic damping treatment. Based on a modified Fourier-Ritz method, Zhang et al. [23] performed the free vibration and damping analyses of porous functionally graded (FG) sandwich plates with a viscoelastic core and two porous FG face layers. By using Kelvin-Voigt viscoelastic model, Zenkour and El-Shahrany [24] estimated the passive damping characteristics of a magnetostrictive laminated composite sandwich plate with a viscoelastic core.

As for the application of ADM, by using the FE method and the Guyan reduction approach, Nayak et al [25-27] investigated the damping control effect and dynamic stability of a sandwich beam

embedded with the MRE core. Arani et al. [28] studied the free vibration characteristics of a sandwich composite micro-plate with two piezoelectric layers to achieve the active vibration control. They found that the electric and magnetic fields had a contribution to the stability of such the smart system if both fields were applied in suitable directions. Shankar et al. [29] predicted the natural frequency characteristic of a sandwich composite plate with integrated active fiber composite actuators and sensors in a hygrothermal environment. In a framework of external voltage excitation, Mao and Zhang [30] investigated the free and forced vibration behaviors of a piezoelectric composite plate reinforced by uniformly and non-uniformly dispersing graphene platelets. Using a meshless approach, Selim et al. [31] explored the anti-vibration effect of functionally graded multilayer graphene nanoplatelets on the reinforced sandwich composite plate integrated with piezoelectric layers. On the aid of Reddy's third-order shear deformation theory, Vinyas et al. [32] estimated the coupled frequency characteristics of three-phase smart magneto-electro-elastic composite plates with considering the effect of piezoelectric interphase thickness. Soleymani and Arani [33] predicted the natural frequency and loss factor characteristics of a Piezo-MRE sandwich plate with consideration of different magnetic intensities. Bisheh et al. [34] predicted the natural frequencies and modal shapes of a laminated CNT-reinforced composite cylindrical shell integrated with the piezoelectric actuators which are applied in the inner and outer surfaces.

By applying for A&PDM, Balamurugan and Narayanan [35] investigated the active-passive hybrid damping control performance of a cantilever composite beam with the enhanced smart constrained layer damping material based on a FE model. Plattenburg et al. [36] proposed an analytical model for predicting the vibration response of a thin composite plate with side-by-side active and passive damping patches. They also proved that the combination of active and passive damping could lead to an increased vibratory attenuation at a single frequency. Kumar et al. [37] presented a FE model to investigate the control performance of active-passive damping of a thin graphite-wafers sandwich composite plate with an actively constrained viscoelastic layer over the surface. Rimašauskienė et al. [38] conducted a series of experimental investigations to evaluate the active and passive suppression capacities of a thin composite beam with a macro fiber composite actuator and two external permanent

magnets. Zenkour and El-Shahrany [39] investigated the influence of hygrothermal on the natural frequencies and forced vibrations of a sandwich plate, which includes layers of fiber reinforced and magnetostrictive materials and core of viscoelastic material.

With the increasingly interdisciplinary nature, an IMAS design approach tends to become a new research hotspot, which facilitates the invention of new-typed multifunctional composite structures. In recent years, some scholars have made a great progress in this field. For example, Kalamkarov et al. [40] proposed a micromechanical design approach for smart composite shells with the application of honeycomb sandwich structures that are embedded by a large number of actuators. Georgiades et al. [41] designed a smart composite shell structure reinforced with a grid of orthotropic actuators. They also proved that the changing of certain geometric or physical parameters could adjust the static and dynamic properties of the smart composite structure. Dyniewicz et al. [42] proposed a semi-active control method to study the forced vibration of a three-layered sandwich elastomer composites beam with MRE core. Felipe, Eloy and their research team [43-44] invented a new composite sandwich beam with 3D printed honeycomb core filled with MRE. They also measured the natural frequencies and response amplitudes of the beam in different external magnetic fields. Based on an integrated design concept of a 3D printed hexagonal reconfigurable element embedded with the shape memory alloy spring, Zhao et al. [45] proposed a reversible and remote controllable reconfigurable structure to maintain a good stiffness property during the actuation process. Tao et al. [46] invented an integrated and versatile design approach for a smart reconfigurable lattice structure with bi-directional corrugated core, and verified the feasibility of the design by comparing the folding/unfolding simulation results with experimental ones.

To date, no comprehensive study has been reported on the composite sandwich plate structure with grille functional core, which makes a good use of a local MRE material for active and passive vibration control via an internal magnetic field excitation based on vibration perception signal. Aiming at filling this gap, an analytical model is proposed to predict the free vibration and damping characteristics of the CFRP-GFB-GFU plate, which can be fabricated based on an IMAS design approach. The plate consists of the CFRP upper and lower skin panels and a grille functional core with

the embedded GFBs and GFUs to meet the requirements of vibration sensing and control functions and to offer the relatively high stiffness and lightweight properties. After the corresponding vibration parameters are successfully solved, both numerical and measured results are utilized to validate the model developed. Finally, the parametric study is conducted to achieve some new analysis findings, which provides the important reference for better exerting vibration suppression performance of such a highly integrated sandwich structure.

2. Integrated material and structure design approach of the CFRP-GFB-GFU plate

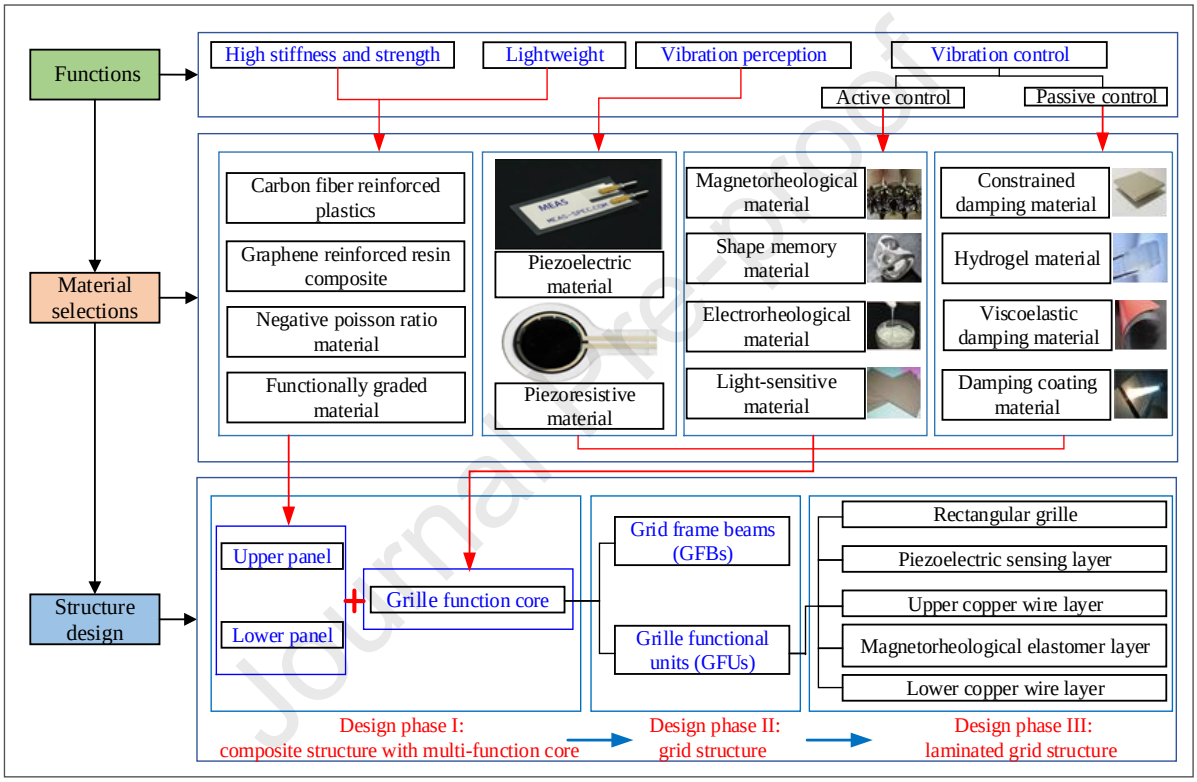

Fig. 1. Schematic diagram of integrated design process of the CFRP-GFB-GFU plate structure.

An integrated design process of the CFRP-GFB-GFU plate is illustrated in Fig. 1, which is divided into three key steps. The first one is to clarify the functional requirements of this new composite structure to be designed, including high stiffness and strength, lightweight, vibration perception, active and passive control, etc. In the second step, the smart composite materials available in the market that meet the above functional requirements are selected, with the cost, processing conditions, performance, reliability being taken into account. The final step is to complete structural design that can turn the desired functions and constituent materials into a highly integrated state. Also, several important design

stages need to be determined and predefined, with some important design variables, such as geometry, fabrication, mechanical and/or physical parameters being comprehensively considered in those design stages, as shown in Fig. 2.

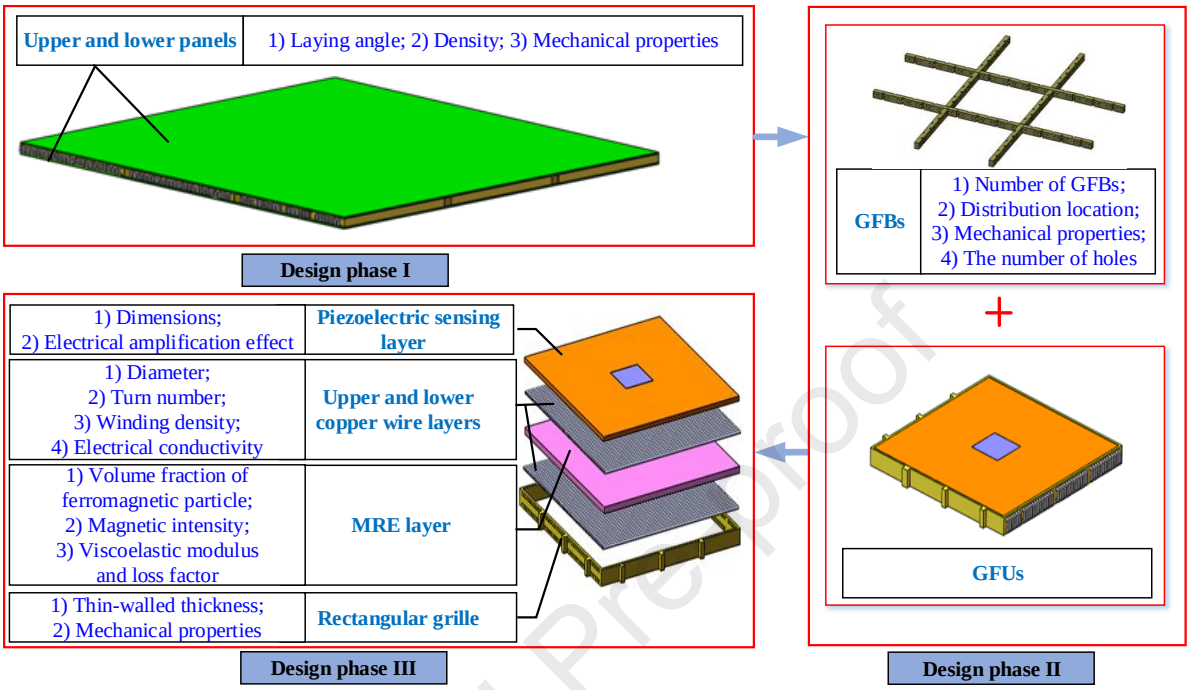

Fig. 2. The design variables in different design phases of CFRP-GFB-GFU laminated structure.

3. Theory and formulation

3.1 Model description

Fig. 3 displays an analytical model of the CFRP-GFB-GFU plate, which consists of the upper and lower CFRP panels and one grille functional core with length *l*, width *d* and thickness *h*. Firstly, at the mid-plane of the lower panel, a global coordinate is established, in which the corresponding coordinates along with length, width and thickness are assumed to be *x*, *y* and *z*, respectively. The grille functional core includes several GFBs and GFUs via falcon riveting connections to obtain vibration sensing and damping control. For the GFBs, the total number of those beams along with *x* and *y* directions are denoted by n_x and n_y, respectively. For the GFUs, each unit is composed of a rectangular grille and several embedded functional materials with 4-layer laminates, including a piezoelectric sensing layer, an upper copper wire layer, an MRE layer and a lower copper wire layer from top to bottom of this type of laminates. Therefore, the total number n_u of GFUs has an explicit relation with n_x and n_y in a determined expression of $n_u = (n_x + 1) \times (n_y + 1)$. Moreover, suppose that there is a local coordinate

system in the CFRP panel, of which '1', '2' and '3' represent three principal material directions of fiber-reinforced composites respectively, θ_f is an angle between the '1' direction and the *x*-axis and n_f is the total number of CFRP layers. The subscripts of '*f*', '*p*', '*c*' and '*v*' are adopted to represent CFRP, piezoelectric sensing material, copper wire, and MRE, while the subscripts of '*gb*' and '*gf*' represent GFB and RG materials. In addition, considering the high preparation cost of piezoelectric sensing layer, it is replaced by a combination of a rectangular piezoelectric film (PF) and high-performance resin material (HPRM) in the sample preparation process. Thus, the subscripts '*pp*' and '*pr*' are adopted to denote the commercial PF and HPRM. Based on the above subscripts, the corresponding length, width, thickness and density of those constituent materials are denoted by l_j, d_j, h_j, ρ_j $(j = f, pp, pr, c, v, gb, gf)$.

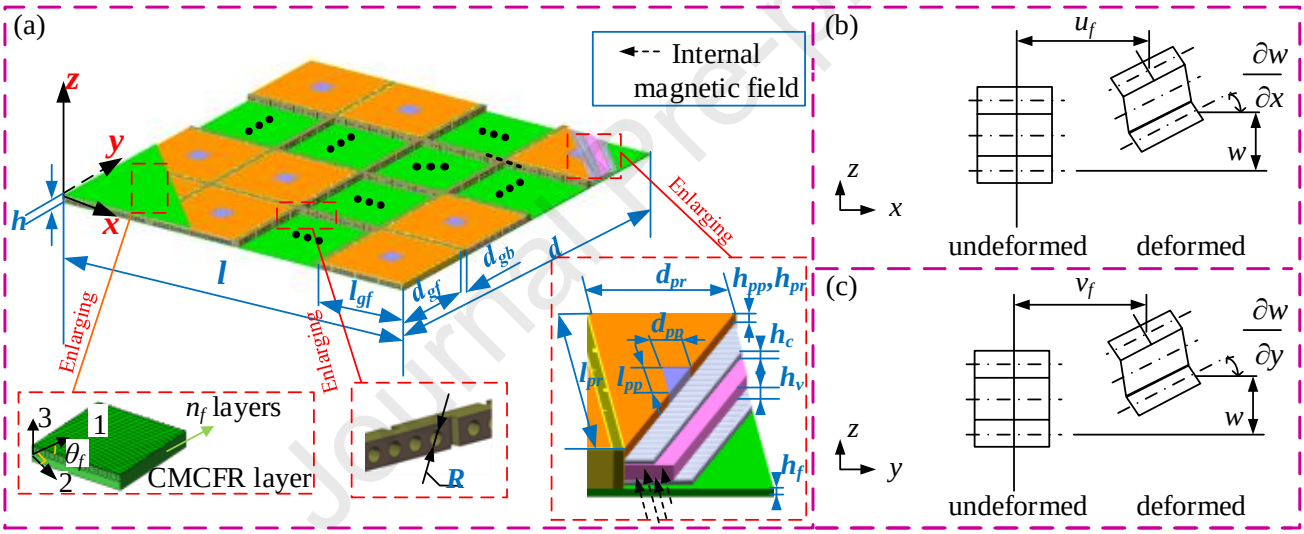

Fig. 3. An analytical model of the CFRP-GFB-GFU plate.

In the modelling process, some assumptions need to be firstly clarified:

(1) Each layer of the CFRP-GFB-GFU structure is boned tightly without relative slippage;

(2) There is no relative deformation between each GFB as well as each layer in GFU;

(3) The magnetic field intensity of MRE in each GFU generated by current-carrying wire layers is proportional to the magnitude of current;

(4) The coupling effects between the magnetic fields related to different MRE layers in GFUs are ignored;

(5) The coupling effect between magnetic field of MRE and very weak electric field generated by the commercial PF in each GFU is ignored.

3.2 Energy expression of GFUs

Based on a new integral first-order shear lamination theory [47-48], the displacement field function of the CFRP-GFB-GFU plate studied is expressed as

$$\begin{aligned} u^{j'}(x,y,z,t) &= u_0^{j'}(x,y,t) + z\varphi_x^{j'}(x,y,t) = u_0^{j'}(x,y,t) - z\frac{\partial \theta^{j'}}{\partial x} \\ v^{j'}(x,y,z,t) &= v_0^{j'}(x,y,t) + z\varphi_y^{j'}(x,y,t) = v_0^{j'}(x,y,t) - z\frac{\partial \theta^{j'}}{\partial y} \quad \left(j' = f,\ p,\ c,\ v,\ gf,\ gb\right) \\ w^{j'}(x,y,z,t) &= w_0^{j'}(x,y,t) \end{aligned} \tag{1}$$

where $u_0^{j'},\ v_0^{j'},\ w_0^{j'}$ $\left(j' = f,\ p,\ c,\ v,\ gf,\ gb\right)$ are the mid-plane displacements of constituent layers or elements of the CFRP-GFB-GFU plate; $\theta^{j'}$ is the rotation value in the global coordinate; $\varphi_x^{j'}$ and $\varphi_y^{j'}$ are the rotation values of the transverse normal in the *xoz* and *yoz* planes; *t* is time.

For the *i*-th GFU, the mid-plane displacement vector $\boldsymbol{\delta}_i^k$ in the *k*-th layer is

$$\boldsymbol{\delta}_i^k = \left[u_{i0}^k(t), v_{i0}^k(t), w_{i0}^k(t), \varphi_{ix}^k(t), \varphi_{iy}^k(t)\right]^{\mathrm{T}} \quad \left(k = p,\ c,\ v,\ gf\right)\ (i = 1, 2, \cdots n_u) \tag{2}$$

where $u_{i0}^k,\ v_{i0}^k,\ w_{i0}^k$ are the mid-plane displacement related to the *k*-th layer and the *i*-th unit; φ_{ix}^k and φ_{iy}^k are the corresponding rotations.

Then, the expressions of stiffness matrices $\boldsymbol{K}_i^k\ (k = k',\ v)$ in the *i*-th GFU are given by

$$\boldsymbol{K}_i^{k'} = \iiint_{-\frac{h_{k'}}{2}}^{\frac{h_{k'}}{2}} \boldsymbol{B}_\tau^{\mathrm{T}} \begin{bmatrix} \bar{Q}_{11}^{k'} & \bar{Q}_{12}^{k'} & 0 \\ \bar{Q}_{21}^{k'} & \bar{Q}_{22}^{k'} & 0 \\ 0 & 0 & \bar{Q}_{66}^{k'} \end{bmatrix} \boldsymbol{B}_\tau \mathrm{d}z\mathrm{d}x\mathrm{d}y \ (k' = p,\ c,\ gf) \tag{3a}$$

$$\boldsymbol{K}_i^{v} = \iiint_{-\frac{h_v}{2}}^{\frac{h_v}{2}} \boldsymbol{B}_\tau^{\mathrm{T}} \begin{bmatrix} \bar{Q}_{11}^{v} & \bar{Q}_{12}^{v} & 0 \\ \bar{Q}_{21}^{v} & \bar{Q}_{22}^{v} & 0 \\ 0 & 0 & \bar{Q}_{66}^{v} \end{bmatrix} \boldsymbol{B}_\tau \mathrm{d}z\mathrm{d}x\mathrm{d}y + \frac{h_v}{\alpha} \iint \boldsymbol{B}_\gamma^{\mathrm{T}} \begin{bmatrix} \bar{Q}_{44}^{v} & 0 \\ 0 & \bar{Q}_{55}^{v} \end{bmatrix} \boldsymbol{B}_\gamma \mathrm{d}x\mathrm{d}y \tag{3b}$$

where $\boldsymbol{B}_\tau$ is the displacement matrix in the *xoy* plane, $\boldsymbol{B}_\gamma$ is the displacement matrix in the *xoz* and *yoz* planes; α is the shear correction factor.

For GFUs, the elements $Q_{mn}^k\ (m, n = 1, 2, 4, 5, 6)$ of $\boldsymbol{K}_i^k$ are described as follows.

$$\bar{Q}_{11}^{p}=\bar{Q}_{22}^{p}=\frac{E_p}{1-v_p^2},\ \bar{Q}_{12}^{p}=\bar{Q}_{21}^{p}=\frac{v_pE_p}{1-v_p^2},\ \bar{Q}_{66}^{p}=\frac{E_p}{2(1+v_p)} \tag{4a}$$

$$\bar{Q}_{11}^{v}=\bar{Q}_{22}^{v}=\frac{E_v}{1-v_v^2},\ \bar{Q}_{12}^{v}=\bar{Q}_{21}^{v}=\frac{v_vE_v}{1-v_v^2},\ \bar{Q}_{44}^{v}=\bar{Q}_{55}^{v}=G_{v23},\ \bar{Q}_{66}^{v}=G_{v12} \tag{4b}$$

$$\bar{Q}_{11}^{c}=\frac{E_{c1}}{1-v_{c12}v_{c21}},\ \bar{Q}_{12}^{c}=\bar{Q}_{21}^{c}=\frac{v_{c12}E_{c2}}{1-v_{c12}v_{c21}},\ \bar{Q}_{22}^{c}=\frac{E_{c2}}{1-v_{c12}v_{c21}},\ \bar{Q}_{66}^{c}=G_{c12} \tag{4c}$$

$$\bar{Q}_{11}^{gf}=\frac{E_{gf}}{1-v_{gf}{}^2},\ \bar{Q}_{12}^{gf}=\bar{Q}_{21}^{gf}=\frac{v_{gf}E_{gf}}{1-v_{gf}{}^2},\ \bar{Q}_{22}^{gf}=\frac{E_{gf}}{1-v_{gf}{}^2},\ \bar{Q}_{66}^{gf}=\frac{E_{gf}}{2(1+v_{gf})} \tag{4d}$$

where E_p and v_p represent the Young's modulus and Poisson ratio of the piezoelectric sensing layer. Note that this layer consists of the commercial PF and HPRM, and E_{pp}, E_{pr} and v_{pp}, v_{pr} are adopted to denote the corresponding moduli and Poisson ratios of the constituent materials. Moreover, E_{c1}, E_{c2}, G_{c12}, v_{c12} and v_{c21} represent the Young's moduli, shear modulus and Poisson ratios of the copper wire layers; E_v and v_v represent the corresponding moduli and Poisson ratio of the MRE layer; E_{gf} and v_{gf} are the ones of the RG.

To consider the damping effect, the complex modulus method [49-50] is adopted to express the complex elastic moduli of the copper wire layers with the following forms

$$\begin{aligned} E_{c1}^{*}&=E_{c1}(1+\mathrm{I}\eta_{c1})\\ E_{c2}^{*}&=E_{c2}(1+\mathrm{I}\eta_{c2})\\ G_{c12}^{*}&=G_{c12}(1+\mathrm{I}\eta_{c12}) \end{aligned} \tag{5}$$

where E_{c1}^{*}, E_{c2}^{*} and G_{c12}^{*} are the complex Young's moduli and shear modulus of the copper wire layer, and η_{c1}, η_{c2} and η_{c12} are the corresponding loss factors.

Similarly, by combing the complex modulus method with the polynomial expansion approach [51-53], the complex shear modulus G_{v12}^{*} of the MRE layer is constructed as

$$G_{v12}^{*}=G_{v12}(1+\mathrm{I}\eta_{v12})=(a_0+a_1B+a_2B^2+\cdots+a_{n_0}B^{n_0})[1+\mathrm{I}(b_0+b_1B+b_2B^2+\cdots+b_{n_0}B^{n_0})] \tag{6}$$

where $\mathrm{I}=\sqrt{-1}$, η_{v12} is the loss factor of the MRE layer, $a_1, a_2, \ldots, a_{n_0}$ and $b_1, b_2, \ldots, b_{n_0}$ are the polynomial fitting coefficients when internal magnetic field is considered, n_0 is the maximum of polynomial order, and B is magnetic induction intensity that is closely related to current magnitude

applied on the current-carrying copper wire layers (the detailed expression of B can be seen in Ref. [50]).

For the *i*-th GFU, the kinetic energy T_{si}^{*} and potential energy U_{si}^{*} are stated as

$$T_{si}^{*}=\frac{1}{2}\dot{\boldsymbol{\delta}}_i^{gf\mathrm{T}}\boldsymbol{M}_i^{gf}\dot{\boldsymbol{\delta}}_i^{gf}+\frac{1}{2}\dot{\boldsymbol{\delta}}_i^{p\mathrm{T}}\boldsymbol{M}_i^{p}\dot{\boldsymbol{\delta}}_i^{p}+\dot{\boldsymbol{\delta}}_i^{c\mathrm{T}}\boldsymbol{M}_i^{c}\dot{\boldsymbol{\delta}}_i^{c}+\frac{1}{2}\dot{\boldsymbol{\delta}}_i^{v\mathrm{T}}\boldsymbol{M}_i^{v}\dot{\boldsymbol{\delta}}_i^{v} \tag{7}$$

$$U_{si}^{*}=\frac{1}{2}\boldsymbol{\delta}_i^{gf\mathrm{T}}\boldsymbol{K}_i^{gf}\boldsymbol{\delta}_i^{gf}+\frac{1}{2}\boldsymbol{\delta}_i^{p\mathrm{T}}\boldsymbol{K}_i^{p}\boldsymbol{\delta}_i^{p}+\boldsymbol{\delta}_i^{c\mathrm{T}}\boldsymbol{K}_i^{c}\boldsymbol{\delta}_i^{c}+\frac{1}{2}\boldsymbol{\delta}_i^{v\mathrm{T}}\boldsymbol{K}_i^{v}\boldsymbol{\delta}_i^{v} \tag{8}$$

where $\dot{\boldsymbol{\delta}}_i^{k}$ is the derivative of mid-plane displacement of the *k*-th layer, and $\boldsymbol{M}_i^{k}$ is the corresponding mass matrix. In this way, the total kinetic energy T_s^{*} and potential energy U_s^{*} for GFUs can be further obtained, which are provided in Eqs. (A.1) and (A.2) of Appendix A.

3.3 Energy expression of GFBs of the grille functional core

For the i_x-th GFB of the CFRP-GFB-GFU plate, its mid-plane displacement $\boldsymbol{\delta}_{i_x}^{gb}$ in the *x* direction is defined as

$$\boldsymbol{\delta}_{i_x}^{gb}=\left[u_{i_x0}^{gb}(t),w_{i_x0}^{gb}(t),\varphi_{i_xy}^{gb}(t)\right]^{\mathrm{T}} \tag{9}$$

where $u_{i_x0}^{gb}$, $w_{i_x0}^{gb}$ and $\varphi_{i_xy}^{gb}$ are the mid-plane displacement and rotation components of the i_x-th GFB.

Then, the stiffness matrix $\boldsymbol{K}_{i_x}^{gb}$ and mass matrix $\boldsymbol{M}_{i_x}^{gb}$ of the i_x-th GFB in the *x* direction are described as

$$\boldsymbol{K}_{i_x}^{gb}=\iiint_{-\frac{h_{gb}}{2}}^{\frac{h_{gb}}{2}}E_{gb}\boldsymbol{B}_{kgb}^{\mathrm{T}}\boldsymbol{B}_{kgb}\mathrm{d}z\mathrm{d}x\mathrm{d}y+\int\frac{G_{gb12}A_{gb}}{\alpha}\boldsymbol{B}_{\gamma gb}^{\mathrm{T}}\boldsymbol{B}_{\gamma gb}\mathrm{d}x \tag{10}$$

$$\boldsymbol{M}_{i_x}^{gb}=\int\begin{bmatrix}A_{gb} & & \\ & A_{gb} & \\ & & I_{gb}\end{bmatrix}\rho_{gb}\Phi^{2}\mathrm{d}x \tag{11}$$

where E_{gb} and G_{gb12} are the Young's and shear moduli of the GFB material, $\boldsymbol{B}_{kgb}$ is the displacement matrix in the *xoy* plane, $\boldsymbol{B}_{\gamma gb}$ is the displacement matrix in *yoz* plane, A_{gb} and I_{gb} are the cross sectional area and moment of inertia, and Φ is the displacement function.

By employing the modified differential quadrature method [54], the stiffness matrix $\boldsymbol{K}_{i_y}^{gb}$ and mass matrix $\boldsymbol{M}_{i_y}^{gb}$ in the y direction of the i_y-th GFB can be formulated as

$$\boldsymbol{K}_{i_y}^{gb} = \iiint_{-\frac{h_{gb}}{2}}^{\frac{h_{gb}}{2}} E_{gb} \boldsymbol{B}_{kgb}^{\mathrm{T}} \boldsymbol{B}_{kgb} \mathrm{d}z\mathrm{d}x\mathrm{d}y + \int \frac{G_{gb12} A_{gb}}{\alpha} \boldsymbol{B}_{\gamma gb}^{\mathrm{T}} \boldsymbol{B}_{\gamma gb} \mathrm{d}y \tag{12}$$

$$\boldsymbol{M}_{i_y}^{gb} = \int \begin{bmatrix} A_{gb} & & \\ & A_{gb} & \\ & & I_{gb} \end{bmatrix} \rho_{gb} \Phi^2 \mathrm{d}y \tag{13}$$

Thus, the total kinetic energy T_{gb}^* and potential energy U_{gb}^* for GFBs of the plate studied are expressed as

$$T_{gb}^* = \sum_{i_x=1}^{n_x} \frac{1}{2} \dot{\boldsymbol{\delta}}_{i_x}^{gb\mathrm{T}} \boldsymbol{M}_{i_x}^{gb} \dot{\boldsymbol{\delta}}_{i_x}^{gb} + \sum_{i_y=1}^{n_y} \frac{1}{2} \dot{\boldsymbol{\delta}}_{i_y}^{gb\mathrm{T}} \boldsymbol{M}_{i_y}^{gb} \dot{\boldsymbol{\delta}}_{i_y}^{gb} \tag{14}$$

$$U_{gb}^* = \sum_{i_x=1}^{n_x} \frac{1}{2} \boldsymbol{\delta}_{i_x}^{gb\mathrm{T}} \boldsymbol{K}_{i_x}^{gb} \boldsymbol{\delta}_{i_x}^{gb} + \sum_{i_y=1}^{n_y} \frac{1}{2} \boldsymbol{\delta}_{i_y}^{gb\mathrm{T}} \boldsymbol{K}_{i_y}^{gb} \boldsymbol{\delta}_{i_y}^{gb} \tag{15}$$

where $\boldsymbol{\delta}_{i_y}^{gb}$, $\dot{\boldsymbol{\delta}}_{i_x}^{gb}$ and $\dot{\boldsymbol{\delta}}_{i_y}^{gb}$ are the mid-plane displacement and its derivatives in the x and y directions.

3.4 Energy expression of the upper and lower panels

For the upper and lower panels, the mid-plane displacement vector $\boldsymbol{\delta}^f$ is defined as

$$\boldsymbol{\delta}^f = \left[u_0^f(t), v_0^f(t), w_0^f(t), \varphi_x^f(t), \varphi_y^f(t) \right]^{\mathrm{T}} \tag{16}$$

Then, the expressions of stiffness matrices $\boldsymbol{K}^f$ in the panels are given by

$$\boldsymbol{K}^f = \iiint_{-\frac{h_f}{2}}^{\frac{h_f}{2}} \boldsymbol{B}_{\tau f}^{\mathrm{T}} \begin{bmatrix} \bar{Q}_{11}^f & \bar{Q}_{12}^f & 0 \\ \bar{Q}_{21}^f & \bar{Q}_{22}^f & 0 \\ 0 & 0 & \bar{Q}_{66}^f \end{bmatrix} \boldsymbol{B}_{\tau f} \mathrm{d}z\mathrm{d}x\mathrm{d}y \tag{17}$$

where $\boldsymbol{B}_{\tau f}$ is the displacement matrix of the panels in the *xoy* plane, and $\boldsymbol{B}_{\gamma f}$ is the displacement matrix of the panels in the *xoz* and *yoz* planes;

For CFRPs, the elements $Q_{mn}^f \ (m,n=1,2,4,5,6)$ of $\boldsymbol{K}^f$ are described as follows.

$$\bar{Q}_{11}^f = \frac{E_{f1}}{1-\nu_{f12}\nu_{f21}},\ \bar{Q}_{12}^f = \bar{Q}_{21}^f = \frac{\nu_{f12}E_{f2}}{1-\nu_{f12}\nu_{f21}},\ \bar{Q}_{22}^f = \frac{E_{f2}}{1-\nu_{f12}\nu_{f21}},\ \bar{Q}_{66}^f = G_{f12} \tag{18}$$

where E_{f1}, E_{f2}, G_{f12}, ν_{f12} and ν_{f21} represent the Young's moduli, shear modulus and Poisson ratios of

the CFRP panels.

The complex elastic moduli of the panels can be expressed in the following forms

$$\begin{aligned} E_{f1}^{*} &= E_{f1}(1+\mathrm{I}\eta_{f1}) \\ E_{f2}^{*} &= E_{f2}(1+\mathrm{I}\eta_{f2}) \\ G_{f12}^{*} &= G_{f12}(1+\mathrm{I}\eta_{f12}) \end{aligned} \tag{19}$$

where E_{f1}^{*}, E_{f2}^{*} and G_{f12}^{*} are the complex Young's moduli and shear modulus of the panels, and η_{f1}, η_{f2} and η_{f12} are the corresponding loss factors.

By referring to Refs. [55-57], the total kinetic energy T_f^{*} and potential energy U_f^{*} for the upper and lower panels are written as

$$T_f^{*} = \dot{\boldsymbol{\delta}}^{f\mathrm{T}} \boldsymbol{M}^{f} \dot{\boldsymbol{\delta}}^{f} \tag{20}$$

$$U_f^{*} = \boldsymbol{\delta}^{f\mathrm{T}} \boldsymbol{K}^{f} \boldsymbol{\delta}^{f} \tag{21}$$

where $\boldsymbol{\delta}^{f}$ and $\dot{\boldsymbol{\delta}}^{f}$ are the mid-plane displacement and its derivative in the panels, and $\boldsymbol{M}^{f}$ and $\boldsymbol{K}^{f}$ are the mass and stiffness matrices.

3.5 Solutions of free vibration and damping properties

Here, to solve the free vibration of the CFRP-GFB-GFU plate, the total kinetic energy T^{*} and potential energy U^{*} are expressed as

$$T^{*} = T_s^{*} + T_{gb}^{*} + T_f^{*} \tag{22}$$

$$U^{*} = U_s^{*} + U_{gb}^{*} + U_f^{*} \tag{23}$$

Furthermore, by using the improved Rayleigh-Ritz method [22], the displacement $w(x,y,t)$ of the CFRP-GFB-GFU plate can be stated as

$$w(x,y,t) = \sum_{m=1}^{M}\sum_{n=1}^{N} A_{mn} P_m(\alpha) P_n(\beta) \sin(\omega t) \tag{24}$$

where m and n are the half wavenumber of modal shapes along x and y directions; M and N are the truncated coefficient, which represent the maximum values of m and n; A_{mn} is the shape coefficient; $P_m(\alpha)$ and $P_n(\beta)$ are the modal functions along the x and y directions that are shown in Eqs. (B.1) and (B.2) of Appendix B.

Then, set $\sin(\omega t)=1$ in Eq. (24), the Lagrange energy function L can be obtained as follows.

$$L = T^* - U^* \tag{25}$$

By minimizing the partial derivative of L with the respect to A_{mn}, one has

$$\frac{\partial L}{\partial A_{mn}} = 0\,, \quad m = 1, 2, \ldots, M\,, \quad n = 1, 2, \ldots, N\,. \tag{26}$$

By substituting Eqs. (22), (23) and (25) into Eq. (26), the characteristic equation can be obtained

$$(\boldsymbol{K} - \omega_i^2 \boldsymbol{M})\boldsymbol{q} = \boldsymbol{0} \tag{27}$$

where $\boldsymbol{K}$ and $\boldsymbol{M}$ are the total stiffness and mass matrices, and $\boldsymbol{q}$ is an eigenvalue. When ignoring the imaginary part of $\boldsymbol{K}$, the natural frequency related to the i-th mode ω_i can be solved. Once ω_i is obtained, modal shape associated with each mode can also be obtained by solving the eigenvalue problem.

Finally, according to the strain energy method [58], the i-th damping ratio ξ_i of the CFRP-GFB-GFU plate can be obtained as

$$\xi_i = \frac{1}{4\pi} \times \frac{\Delta U_i}{U_i} \tag{28}$$

where U_i and ΔU_i are the strain energy and the dissipation energy related to the i-th mode of the CFRP-GFB-GFU plate respectively, with the detailed expressions being provided in Eqs. (C.1) and (C.2) of Appendix C.

4. Validation

4.1 Numerical validation

4.1.1 Numerical validation of the composite plate with GFBs

Firstly, natural frequency results between the present study and that from Refs. [59-61] are compared to verify the effectiveness of the current model in predicting the free vibration of the composite plate with GFBs. In the calculations, a simply-supported composite plate ([90/0/90]) with GFBs ([90/0]) is adopted, with GFUs being ignored temporarily in the current model. The corresponding parameters are: l=400 mm, d=300 mm, h_f=3.4 mm, d_{gb}=3 mm, h_{gb}=4 mm, n_x=0, n_y=2,

E_{gb}=9.71 GPa, G_{gb12}=0.9025 GPa, and ρ_{gb} =1347 kg/m^3. Note that the material parameters of the plate are regarded to be identical with the ones of GFBs. Meanwhile, the frequency results from Refs. [59-61] are all extracted from Table 3 in literature [59], which are solved based on the FE method. In addition, the present results are calculated by the improved Rayleigh-Ritz method with the truncated coefficients M=N=8. Table 1 lists the comparison of the first four natural frequencies, from which it can be observed that a relatively good agreement between the frequency results calculated by the current model and those obtained from literature [59-61]. The small deviations may be caused by the ignorance of shear moduli in *xoz* and *yoz* planes in the present model.

Table 1. Comparison of first four natural frequencies of the composite plate with GFBs.

Mode order	Chao and Lee. [61]	Behera et al. [60]	Behera et al. [59]	The present
1	58.96	58.27	58.36	58.17
2	95.68	95.65	95.75	95.58
3	205.74	203.33	203.44	202.99
4	235.75	230.06	230.2	230.45

4.1.2 Numerical validation of grille functional core

Secondly, natural frequency results between the present study and Ref. [62] are compared to validate the model developed in predicting the free vibration of the grille functional core. As can be seen in Fig. 1, this core can be regarded as a simply-supported composite plate with multiple rectangular cutouts. As the result, two panels and the 4-layer laminates embedded in all of RGs are ignored in our model with the following geometrical and material parameters: l=400 mm, d=300 mm, l_{pr}=40 mm, d_{pr}=40 mm, E_{gf}=59 MPa, ν_{gf} =0.36, ρ_{gf} =2680 kg/m^3. Table 2 gives the comparison of the first four natural frequencies of the grille functional core with different numbers of rectangular cutouts. A good consistency can be found between those frequency results calculated by different theoretical models, with the deviation of natural frequencies being less than 1.0 %. The deviation is probably due to the ignorance of the boundary potential energy and potential energy related to the coupling force and moment in the present model.

Table 2. Comparison of natural frequencies of the grille functional core with different number of rectangular cutouts.

Number of rectangular cutouts	Source	1 Mode	2 Mode	3 Mode	4 Mode
2	The present /Hz	77.40	160.91	226.32	305.22
	Ref. [62] /Hz	77.77	161.32	228.52	302.43
	Deviation /%	0.5	0.3	1.0	0.9
4	The present /Hz	76.03	160.61	221.44	301.72
	Ref. [62] /Hz	76.79	160.70	222.53	300.35
	Deviation /%	1.0	0.1	0.5	0.5
6	The present /Hz	75.68	158.97	220.91	299.27
	Ref. [62] /Hz	75.72	159.05	221.40	298.00
	Deviation /%	0.1	0.1	0.2	0.4

4.1.3 Numerical validation of the composite plate with MRE

Finally, the results in Ref. [63] are adopted to prove the effectiveness of the present model in predicting both natural frequencies and damping parameters of a simply-supported composite sandwich plate with MRE. Note that MRE is made by the micron sized carbonyl iron particles and non-ferrous (natural rubber) polymeric matrix. In the calculations, two panels, GFBs and RGs, and piezoelectric sensing layer are ignored temporarily in the current model with the geometrical and material parameters being: l_c=l_v=400 mm, d_c=d_v=300 mm, h_v=2 mm, E_{c1}=E_{c2}=72 GPa, ρ_v=3312.7 kg/m^3, ρ_c=2700 kg/m^3, ν_v=0.49 and ν_{c12}=0.3. In addition, the shear modulus and loss factor of MRE are shown in Appendix D. Table 3 lists the comparison of the first three natural frequencies and loss factors of the simply-supported composite sandwich plate with an MRE layer subjected to the external magnetic field with induction intensity ranging from 0 to 0.4 T. It can be observed that the maximum deviation of the first three natural frequencies and modal loss factors are up to 1.9 % and 2.6 %, respectively, which indicates a relatively good agreement. Those deviations probably due to the ignorance of material permeability effect between MRE and the nearby layers in the current model.

Table 3. Comparison of the first three natural frequency and loss factors of the simply-supported composite sandwich plate with an MRE layer under different magnetic inductions.

B /T	Source	Natural frequency /Hz			Modal loss factor		
		1 Mode	2 Mode	3 Mode	1 Mode	2 Mode	3 Mode
0	Ref. [63]	178.97	349.20	485.26	0.0453	0.0246	0.0180

	The present	175.56	346.30	484.97	0.0454	0.0252	0.0177
	Deviation /%	1.9	0.9	0.1	0.2	2.4	1.7
0.2	Ref. [63]	187.92	358.78	495.07	0.0762	0.0432	0.0322
	The present	185.23	357.91	493.19	0.0767	0.0436	0.0324
	Deviation /%	1.4	0.2	0.4	0.7	0.9	0.6
0.4	Ref. [63]	196.91	368.61	505.25	0.0944	0.0533	0.0423
	The present	194.32	366.07	507.29	0.0956	0.0535	0.0434
	Deviation /%	1.3	0.7	0.4	1.3	0.4	2.6

4.2 Experimental validation

4.2.1 Material fabrication and experimental setup

A CFRP-GFB-GFU plate specimen with n_x=1 and n_y=2 (i.e. it has 6 pieces of GFUs) is taken as the test object, whose fabrication flowchart is illustrated in Fig. 4, with the following key steps: (1) silicone oil, iron powder and silicone rubber are adopted to prepare for six rectangular pieces of MRE via a set of picture framed compression molds [50]. In the compression process, each piece of MRE material is solidified with two permanent magnets, which have a very strong magnetic field with magnetic induction intensity approaching 700 mT; (2) alcohol-bonded enameled wire is wrapped with a winding mold (that is pre-designed and can be taken out when this step is completed) and absolute ethanol is used to bond the adjacent enameled wire to obtain six sets of rectangular copper coils; (3) each piezoelectric film is pasted to the outer surface of each set of rectangular copper coils and MRE material is embedded inside. Subsequently, they are packaged into each RG with epoxy adhesive to obtain a desired GFU; (4) when six GFUs are successfully prepared, they are assembled together with three GFBs made by 3D printing technology via falcon riveting connections to obtain a grille functional core; (5) some pieces of carbon fiber cloths purchased are laid up to fabricate a CFRP panel with the laminate scheme of $[0°/90°]_5$ and volume fraction of 55%, which are obtained via the compression and curing process in vacuum environment ; (6) Two CFRP panels are made and respectively laid on both sides of grille functional core to prepare the CFRP-GFB-GFU plate specimen, with resin impregnating into the interface layers in vacuum condition. The geometrical and material parameters of constituent layers of the specimen are shown in Table 4, where the geometrical parameters are measured by Vernier caliper, and material parameters are provided by the manufactures except for the one of MRE, whose Young's modulus, Poisson's ratio and loss factors are referenced from literature [63].

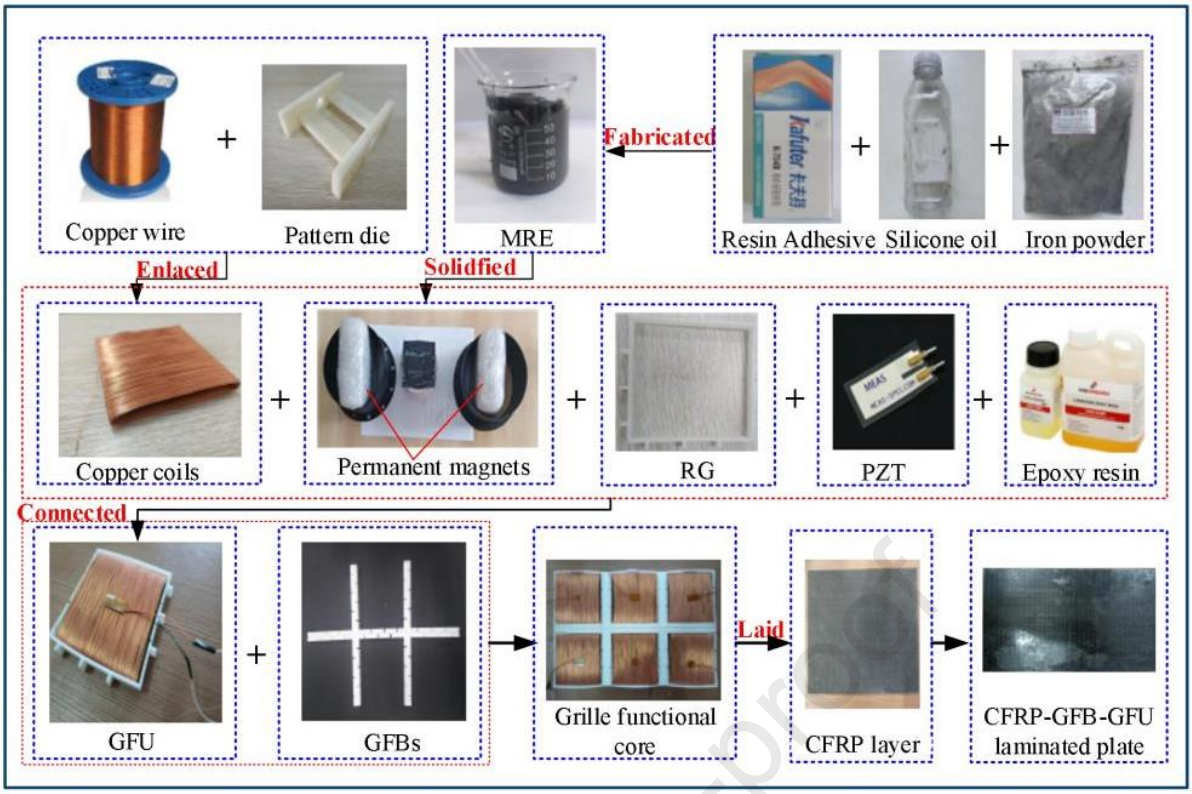

Fig. 4. A flowchart for fabrication of the CFRP-GFB-GFU plate specimen.

Table 4. Geometric and material parameters of constituent layers or elements of the CFRP-GFB-GFU plate specimen.

Type	Parameters
CFRP panel	l=278 mm, d=181 mm, h_f=1 mm, ρ_f =1370 kg/m^3, $E_{f1}=115\times10^3$ MPa, $E_{f2}=9.5\times10^3$ MPa, $G_{f12}=7.1\times10^3$ MPa, $v_f=0.32$
Piezoelectric sensing layer	l_{pr}=80 mm, d_{pr}=80 mm, h_{pr}=1 mm, ρ_{pr} =1940 kg/m^3, l_{pp}=10 mm, d_{pp}=5 mm, h_{pp}=0.1 mm, ρ_{pp}=7500 kg/m^3, $E_{pr}=119\times10^3$ MPa, $E_{pp}=76.5\times10^3$ MPa, $v_{pr}=0.33$, $v_{pp}=0.32$
Copper wire layer	R=0.3 mm, turn number n_c=267, ρ_c =8900 kg/m^3, $E_{c1}=163\times10^3$ MPa, $E_{c2}=143\times10^3$ MPa, $G_{c12}=47.5\times10^3$ MPa, $v_{c12}=0.35$
MRE layer	ρ_v =3300 kg/m^3, $E_v=7.8\times10^3$ MPa, $v_v=0.7$
Rectangular grille	l_{gf}=84 mm, d_{gf}=84 mm, ρ_{gf} =1050 kg/m^3, $E_{gf}=2.2\times10^3$ MPa, $v_{gf}=0.394$
GFB	d_{gb}=13 mm, ρ_{gb} =1050 kg/m^3, $E_{gb}=2.2\times10^3$ MPa, $G_{gb12}=0.567\times10^3$ MPa

The vibration and damping data of the CFRP-GFB-GFU plate specimen with cantilever boundary conditions are measured based on a dynamic experimental system that is set up in a laboratory environment, as shown in Fig. 5. Initially, an impact hammer (PCB 086C01, PCB Piezotronics, US) is used to measure frequency response functions with different excitation points and a fixed response

point that is measured by a lightweight acceleration sensor (BK 4517-001, Brüel & Kjær, Denmark). In the hammer tests, natural frequencies and mode shapes can be obtained via the Polymax method [64] with frequency resolution of 0.1 Hz, transient window for impact excitation signal and exponential window for response signal, where a wireframe testing model with mesh division of 7×9 is established in advance using LMS Test Lab.12b software. Then, a frequency-sweeping testing approach [65] excited with a shaker bench (Dongling ES-80W-445, Dongling Technologies, China) is adopted to obtain the frequency spectrum data (measured by a Polytec PDV-100 laser vibrometer (Polytec GmbH, Gemany) and another BK 4517-001 lightweight acceleration sensor) associated with a sweeping interval that contains each natural frequency [66], where the sweeping speed is 0.5Hz/s and excitation amplitude is selected as 1.0 g. Note that with the measured frequency spectrum data, the damping ratio related to each mode order of the specimen can be identified by the half-power bandwidth method [67] (To ensure the accuracy, only the noncontact response data measured by vibrometer is used for the final damping identification). In addition, the 24V-DC power is used to provide the voltage for single to six sets of rectangular copper coils to generate internal magnetic field for the specimen with different GFU regions, of which the adjustable resistance ranging from 800 to 2400 Ω is connected to control the magnetic field (the related magnetic induction intensity changes from 0 to 180 mT). When the desired magnetic field amplitude is reached, the measurements are completed as soon as possible with all of excitation and response signals being recorded via LMS SCADAS data acquisition instrument, to minimize the thermal effect generated by the continuous magnetic field which is ignored in the present study.

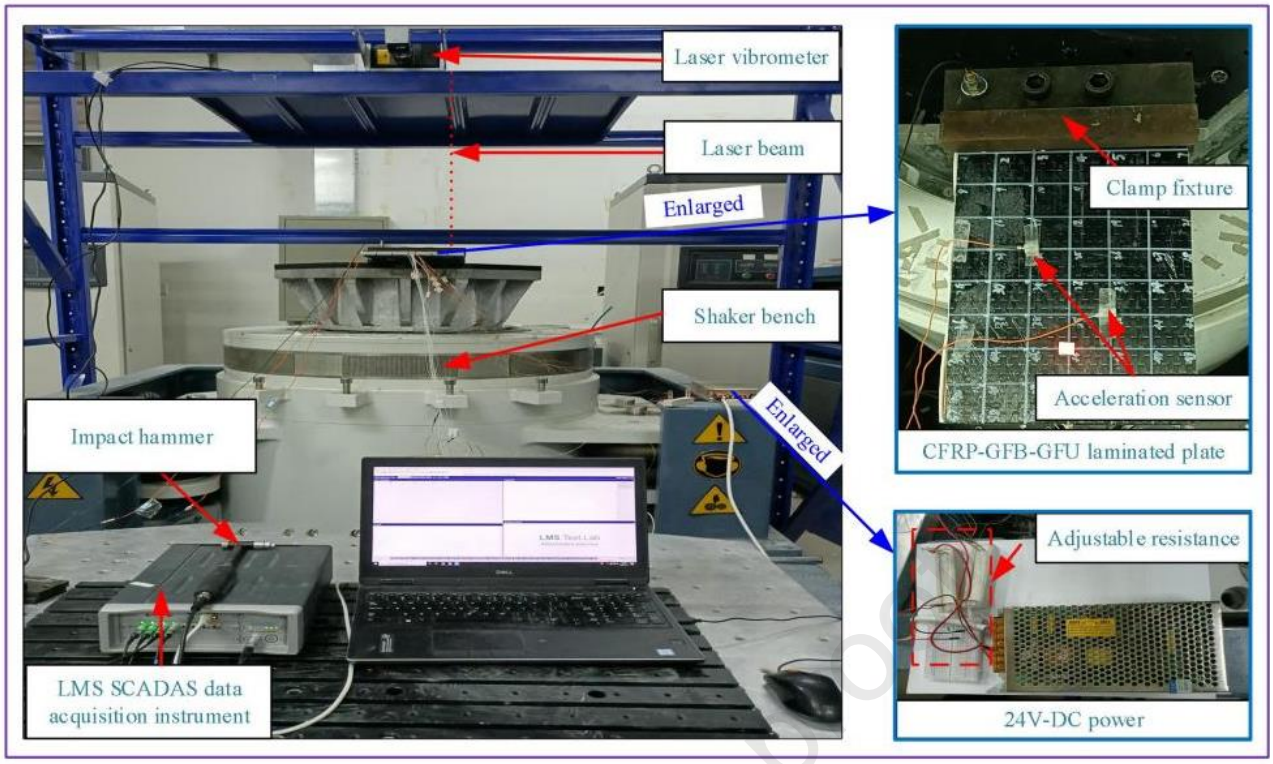

Fig. 5. A dynamic experiment system for the CFRP-GFB-GFU plate specimen.

4.2.2 Measured results with piezoelectric sensing layers in different GFUs

Here, the base vibration energy provided by the shaker bench is applied on the CFRP-GFB-GFU plate specimen with excitation amplitude of 1g and excitation frequency of 80 Hz. Then, several techniques to apply magnetic field are adopted to evaluate the vibration suppression effect. Fig. 6 shows the corresponding time-waveforms perceived at different GFU regions, where the predefined piezoelectric sensing regions are also displayed in the same figure. Note that at this time the magnetic induction intensity of 140 mT is used and the vibration perception signals are obtained via rectangular piezoelectric films powered by the charged amplifier circuit. It can be found that when the internal magnetic field is generated, vibration responses at the regions of GFU-I and GFU-II decrease. Moreover, as the number of GFU region with the controllable magnetic field increases, the vibration results further decrease, which proves that the multifunctional requirements such as lightweight, vibration sensing, active and passive control can be realized by this highly integrated sandwich plate structure.

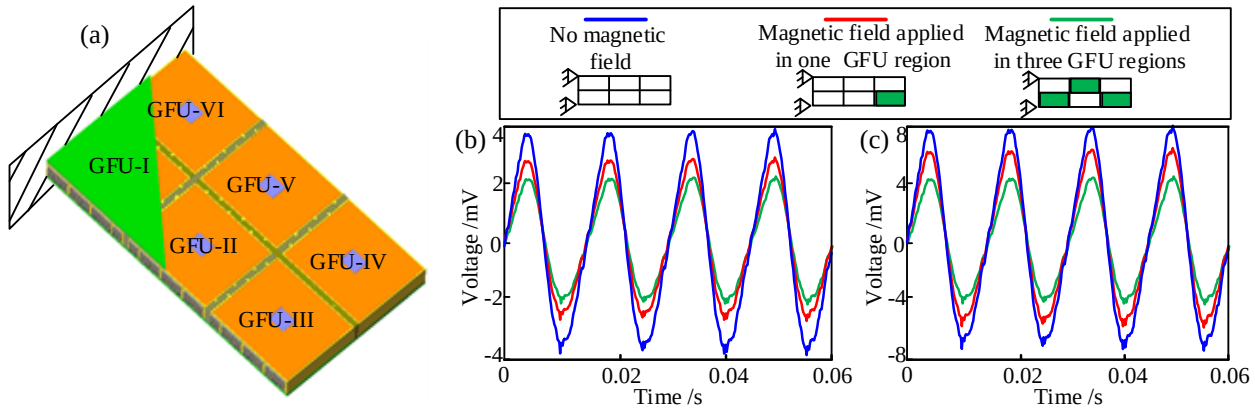

Fig. 6. Diagram of (a) piezoelectric sensing regions of the CFRP-GFB-GFU plate specimen and time-waveforms perceived at the center of (b) GFU-I and (c) GFU-II with different applying techniques of magnetic field.

4.2.3 Comparison of the theoretical and tested results

Table 5 shows the comparison of the first three natural frequencies and damping ratios of the CFRP-GFB-GFU plate specimen with different magnetic induction intensities obtained by theoretical calculations and experimental tests, when the magnetic field is applied in only one GFU region, as already shown in Fig. 6. Moreover, by taking the magnetic induction intensity of 180 mT as an example, Fig. 7 compares the first four natural frequencies and damping ratio results, where different green region represents different magnetic field distribution pattern in the related GFU regions. Besides, Fig. 8 shows the comparison of the calculated and measured modal shapes of the specimen without magnetic field, since the shape results seem to be unchanged no matter how the magnetic induction intensity changes.

Table 5. Comparison of the first three natural frequencies and damping ratios with different magnetic induction intensities obtained by theoretical calculations and experimental tests.

B / mT	Source	Natural frequency /Hz				Damping ratio			
		1 Mode	2 Mode	3 Mode	4 Mode	1 Mode	2 Mode	3 Mode	4 Mode
0	Theoretical	65.72	141.50	408.83	1041.72	0.0702	0.0520	0.0375	0.0217
	Experimental	64.25	140.25	406.25	1037.25	0.0732	0.0503	0.0355	0.0205
	Error /%	2.3	0.9	0.6	0.4	4.3	3.4	5.6	5.8
60	Theoretical	65.74	142.75	411.32	1042.64	0.0759	0.0538	0.0386	0.0231
	Experimental	64.5	140.5	409.5	1038.50	0.0743	0.0525	0.0368	0.0219
	Error /%	2.1	1.6	0.4	0.4	2.2	2.5	4.9	5.5
120	Theoretical	65.75	143.14	413.69	1043.57	0.0773	0.0554	0.0430	0.0258
	Experimental	65.5	141.25	411.25	1039.50	0.0760	0.0532	0.0407	0.0245
	Error /%	0.8	1.3	0.4	0.4	1.7	4.1	5.7	5.3

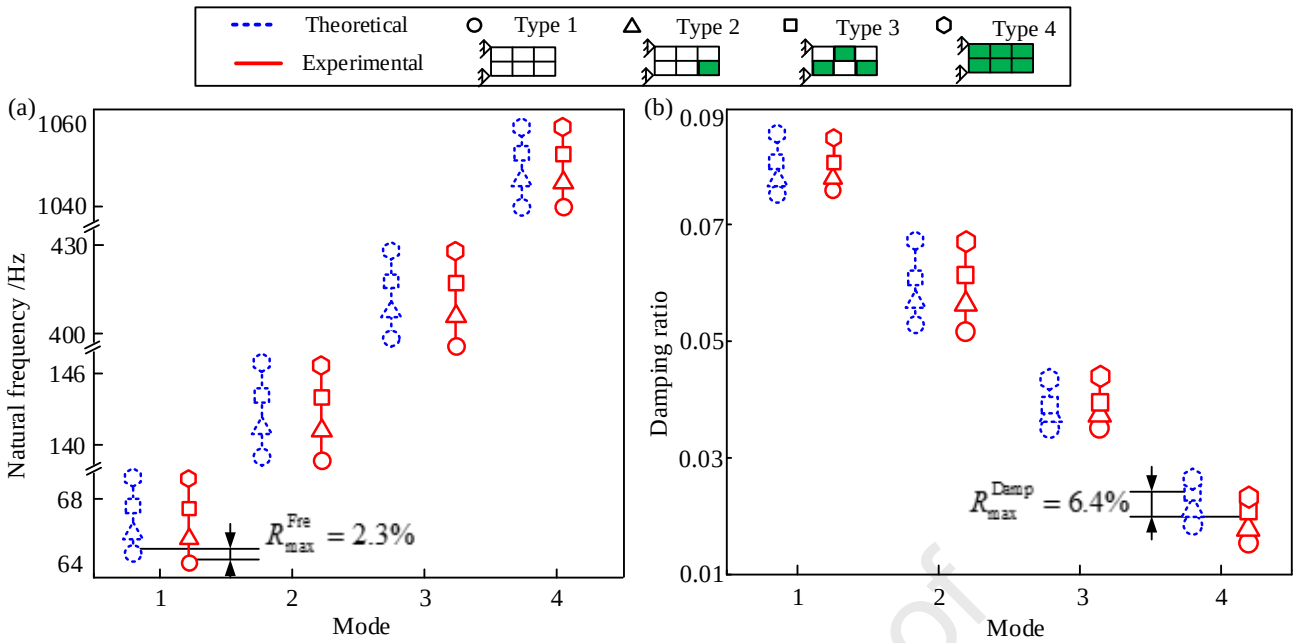

Fig. 7. Comparisons of (a) the first four natural frequencies and (b) damping ratios of the specimen with magnetic induction intensity of 180 mT obtained by theoretical calculations and experimental tests.

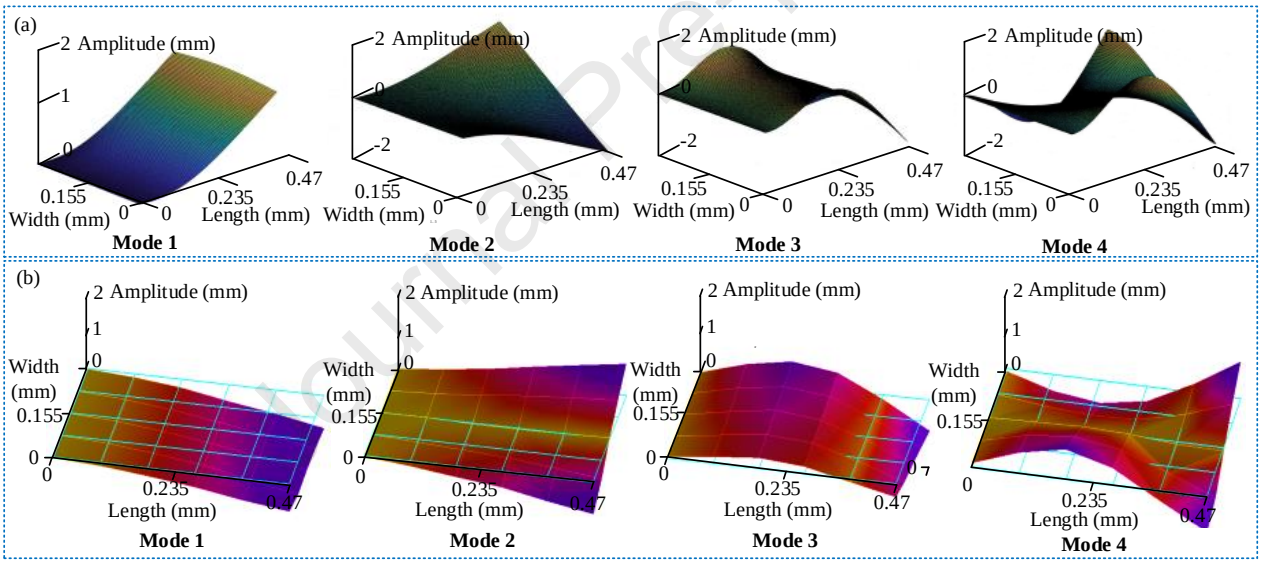

Fig. 8. Comparisons of (a) theoretical and (b) experimental modal shapes of the specimen associated with the first four modes without magnetic field.

The magnetic field dependent behavior of the CFRP-GFB-GFU plate specimen can be clearly seen from Table 5, since both frequency and damping results obtained by theoretical calculations and experimental tests show an upward trend as the magnetic induction intensity increases. Meanwhile, it can be observed from this Table and Figs 7 to 8 that with the increment of controllable magnetic field distribution area, both frequency and damping results become large with the maximum relative errors R_{max}^{Fre} and R_{max}^{Damp} being 2.3 % and 6.4 %, respectively. Moreover, there is a relatively good agreement

between theoretical and experimental modal shape results. Thus, the model developed is trustworthy to predict the dynamic characteristics of multifunctional grille composite sandwich plates.

5. Parametric studies

5.1 Influence of magnetic induction intensity, thickness ratio and magnetic field distribution pattern of MRE in GFUs

Fig. 9 presents the influence of magnetic induction intensity and thickness ratios of the MRE to the overall plate on the normalized natural frequencies and damping ratios associated with the first three modes of the CFRP-GFB-GFU plate. Besides, the corresponding influence of magnetic field distribution patterns (MFDPs) of the local MRE in GFUs is investigated. In the calculations, the geometrical and material parameters of the CFRP-GFB-GFU plate which are different from Table 4 are listed in Table 6 and five different types of MFDP are defined in Fig. 10 with G_{v12}, G_{v23} and η_{v12} of MRE being shown in Ref. [49]. It is worth noting that: (1) when the influence of B (magnetic induction intensity) is investigated, the initial value is set as 0 T with h_v/h= 0.3 and "type 5" in MFDP being chosen; (2) as the variation of h_v/h is analyzed, the initial value is set as 0.1with B=0.3 T and "type 5" in MFDP being chosen; (3) when the variation of MFDP is investigated, the initial pattern is selected as "type 1" with B =0.3 T and h_v/h = 0.3 being chosen. In addition, the maximum relative variations of frequency (namely $F_{\max}$) and damping parameters (namely $D_{\max}$) are also displayed in Fig. 9. In the next discussion, if there is no special explanation, $F_{\max}$ and $D_{\max}$ associated with other influential factors are all obtained and plotted in the related figures.

Table 6. Geometric and material parameters of constituent layers or elements of the plate used in the calculations.

Category	Parameters
CFRP panel	l=470 mm, d=310 mm,
Piezoelectric sensing layer	l_{pr}=151 mm, d_{pr}=150 mm, ρ_{pr} =1618 kg/m^3, l_{pp}=60 mm, d_{pp}=60 mm, h_{pp}=1 mm,
Copper wire layer	R=0.2 mm, turn number n_c=75,
Rectangular grille	l_{gf}=155 mm, d_{gf}=154 mm, ρ_{gf} =1618 kg/m^3, $E_{gf}=119\times10^3$ MPa, $v_{gf}=0.32$
GFB	d_{gb}=2 mm, ρ_{gb} =1420 kg/m^3, $E_{gb}=2600\times10^3$ MPa, $G_{gb12}=93.82\times10^3$ MPa

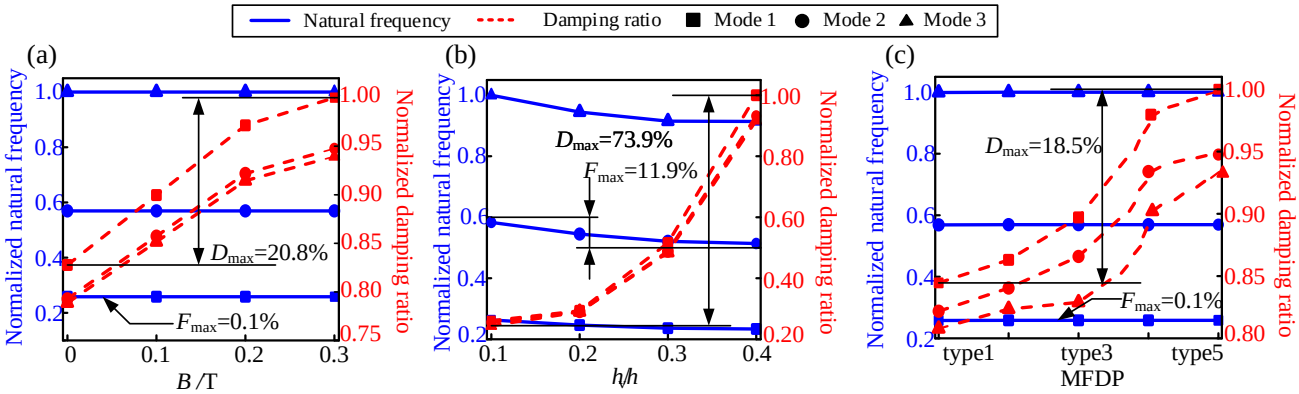

Fig. 9. Influence of (a) magnetic induction intensity, (b) h_v/h and (c) MFDP of the MRE in GFUs on the normalized natural frequencies and damping ratios associated with the first three modes of the CFRP-GFB-GFU plate.

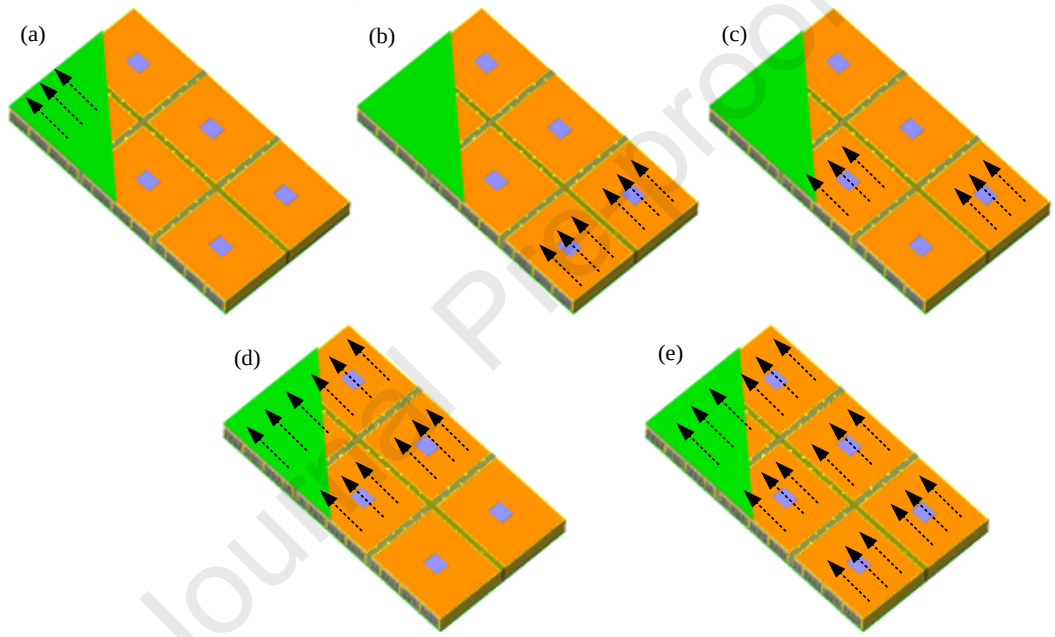

Fig. 10. MFDPs of GFUs with (a) type 1, (b) type 2, (c) type 3, (d) type 4 and (e) type 5.

An examination of Fig. 9 shows that with the increment of the magnetic field energy and type number of MFDP, the first three natural frequencies of the structure system increase slightly due to the increment of shear modulus G_{v12}^{*} in Eq. (6). However, with increasing the h_v/h ratio, the frequency results show an obvious downward trend with the maximum declining degree of 11.9 %, which is caused by the enlargement of structural stiffness since volume ratio of MRE to the overall structure rises. Besides, as those aforementioned factors increase, the corresponding damping parameters of the CFRP-GFB-GFU plate show a clear upward trend with the maximum increasing degree being 20.8, 73.9 and 18.5 %, respectively, which is caused by the increased shear modulus G_{v12}^{*} that leads to the ascending value of dissipation energy. Thus, the larger magnetic field energy and thickness ratio of

MRE are, the higher anti-vibration capability of the CFRP-GFB-GFU plate is. However, to save the energy of magnetic field applied on the specimen, type 4 in MFDP rather than type 5 is recommended for the application of reasonable magnetic field distribution of MRE in GFUs, since there are not many differences between the damping performances of type 4 and type 5 in MFDP (Fig. 10).

5.2 Influence of diameter and number of turn of the copper wire in GFUs

Fig. 11 presents the influence of diameter R and the turn number n_c of the copper wire in GFUs on the normalized natural frequencies and damping ratios associated with the first three modes of the CFRP-GFB-GFU plate. In the calculations, the same geometrical and material parameters provided in Table 5 are selected, with $B = 0.3$ T, $h_v/h = 0.3$, and "type 5" in MFDP being predefined. Besides, when the influence of diameter of the copper wire is discussed, its initial value is set as 0.5 mm with $n_c = 75$ being selected; when the variation of n_c is studied, its initial value is selected as 30 together with $R = 1$ mm.

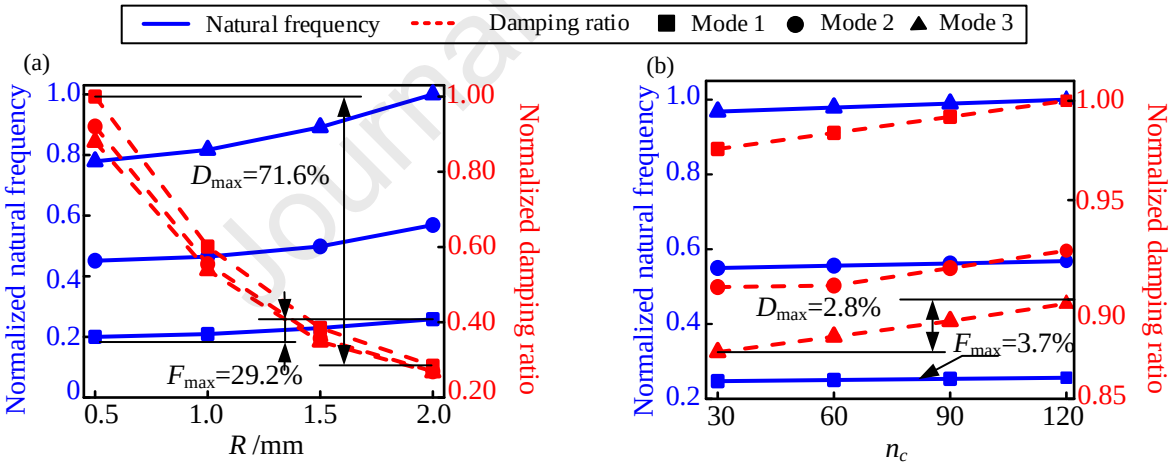

Fig. 11. Influence of (a) the diameter R and (b) turn number n_c of copper wire in GFUs on the normalized natural frequencies and damping ratios associated with the first three modes of the CFRP-GFB-GFU plate.

It can be observed from Fig. 11 that the increment of n_c has a mild influence on both natural frequency and damping ratio of the CFRP-GFB-GFU plate. However, with the rising of R, the frequency parameters show a clear uptrend with the maximum increment of 29.2 %. Meanwhile, the damping parameters have a steep downtrend with the maximum reduction of 71.6 %, which is due to the coupling effects of U and ΔU (usually the increasing degree of U is larger than that of

ΔU) in Eq. (28). Hence, to keep a good balance between damping and stiffness performances, the compromised R value is suggested to be relatively small.

5.3 Influence of volume ratio and distribution pattern of GFBs

Fig. 12 shows the influence of distribution pattern and volume ratio of GFBs to the overall plate on the normalized natural frequencies and damping ratios associated with the first three modes, which is calculated based on the identical geometrical and material parameters adopted in Section 5.2. It is worth noting that: (1) "type 1" presents the distribution pattern of GFBs with n_x=n_y=1; (2) "type 2" denotes the corresponding pattern with n_x=1 and n_y=2; (3) "type 3" presents the one with n_x= n_y=2; (4) "type 4" is the one with n_x=1 and n_y=3. Besides, when the influence of volume ratio of GFBs is investigated, its initial value is chosen as 1.2 % with the distribution of type 2 being selected; When the variation of distribution pattern of GFBs is studied, the corresponding initial value is determined as "type 1" with a volume ratio of 2.4 % being chosen.

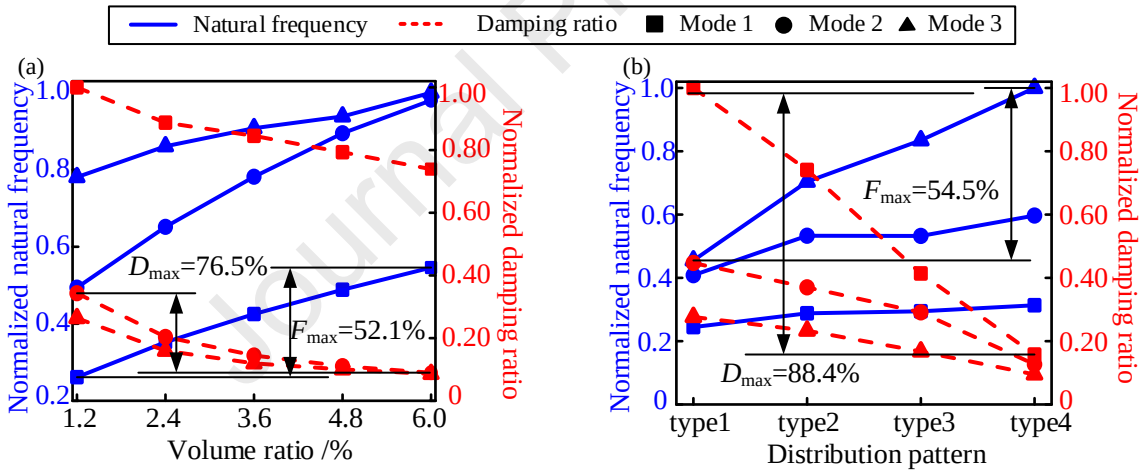

Fig. 12. Influence of (a) volume ratio and (b) distribution pattern of GFBs on the normalized natural frequencies and damping ratios associated with the first three modes of the CFRP-GFB-GFU plate.

It can be observed from Fig. 12 that due to the increase of $\boldsymbol{K}$ in Eq. (27) which is affected by stiffness matrices $K_{i_x}^{gb}$ and $K_{i_y}^{gb}$, as the volume ratio and type number of distribution pattern of GFBs increase, results of natural frequency of the CFRP-GFB-GFU plate display an uptrend with the maximum rising degree being 52.1 % and 54.5 %, respectively. However, the damping parameters show a significant downtrend with the increase of volume ratio and distribution pattern, with the maximum declining degree being 76.5 % and 88.4 %, respectively. Thus, to better exert vibration

suppression capacity and maintain relatively good stiffness performance, it is recommended that volume ratio should be selected from 2.4 % to 3.6 % with the distribution of type 2 of GFBs.

6. Conclusions

In this work, a novel analytical model has been proposed to predict natural frequencies, modal shapes and damping parameters of the CFRP-GFB-GFU plates with relatively high calculation accuracy, which is well validated based on both numerical and experimental results. The model developed well deals with complex multifunctional grille sandwich structure, which can be fabricated based on an integrated material and structure design approach. Moreover, this model can be employed to evaluate the active and passive vibration behaviors whether the controllable internal magnetic field distribution pattern of MRE in GFUs is considered or not.

On the basis of the measured results, it can be found that this multifunctional plate offers a very good passive vibration suppression capacity with the damping ratios associated with the first three modes reach 7.3, 4.7 and 4.2 %, respectively. Meanwhile, its anti-vibration performance can be further improved once the active control strategy is adopted. The damping results indicate that the active vibration suppression performance is proportional to the controllable magnetic field energy applied in GFUs.

Based on the parametric study results, it can be concluded that to better exert vibration suppression capacity and maintain relatively good stiffness performance, small diameter of copper wire and large magnetic induction intensity and thickness ratio of MRE should be adopted. Also, it is suggested to select the reasonable region of magnetic field distribution of MRE in GFUs and distribution pattern and the volume ratio of GFBs to the CFRP-GFB-GFU plate.

This paper has provided an effective analysis model for investigation of free vibration and damping characteristics of the CFRP-GFB-GFU plate subjected to an internal magnetic field excitation, which can be easily extended to other similar composite plate and shell structures. However, it should

be admitted that the coupling effect of multiple local magnetic fields between the nearby GFUs in the grille functional core is ignored, which needs to be considered in future study to have a better understanding of this effect on active vibration suppression performance.

Acknowledgments

The authors would like to thank the financial supports on the current study provided by the National Natural Science Foundation of China (Grant No. 51505070, 51970530 and 12072091); the Science Foundation of the National Key Laboratory of Science and Technology on Advanced Composites in Special Environments (granted No. 6142905192512); the Fundamental Research Funds for the Central Universities of China (Grant No. N2103026); the major projects of aero-engines and gas turbines (J2019-I-0008-0008); the China Postdoctoral Science Foundation (2020M680990).

Conflict of interests

The authors declare that there is no conflict of interests regarding the publication of this paper.

References

[1] H. Xu, L. Zu, B. Zhang, H. You, D. Li, H. Wang, B. Zi, Static and dynamic bending behaviors of carbon fiber reinforced composite cantilever cylinders, Compos. Struct. 201 (2018) 893-901.

[2] B. Safaei, R. M. Dastjerdi, Z. Qin, F. Chu. Frequency-dependent forced vibration analysis of nanocomposite sandwich plate under thermo-mechanical loads. Composites. Part. B. 161 (2019) 44-54.

[3] R. Rani, R. Lal. Free vibrations of composite sandwich plates by Chebyshev collocation technique. Composites. Part. B. 165 (2019) 442-455.

[4] A. Gupta, A. Ghosh. Isogeometric static and dynamic analysis of laminated and sandwich composite plates using nonpolynomial shear deformation theory. Composites. Part. B. 176 (2019) 107295.

[5] H. Li, T. Wu, Z. Gao, X. Wang, H. Ma, Q Han, Z. Qin, An iterative method for identification of temperature and amplitude dependent material parameters of fiber-reinforced polymer composites, Int. J. Mech. Sci. 184 (2020) 105818.

[6] C.A. Geweth, F.S. Khosroshahi, K. Sepahvand, C. Kerkeling, S. Marburg, Damage detection of

fiber-reinforced composite structures using experimental modal analysis, Pro. Eng. 199 (2017) 1900-1905.

[7] H. Li, T. Zhang, Z. Li, B. Wen, Z. Guan, Modeling of the nonlinear dynamic degradation characteristics of fiber-reinforced composite thin plates in thermal environment, Nonlinear. Dyn. 98 (2019) 819-839.

[8] L. S. Yousuf. Nonlinear dynamics investigation of flexural stiffness of composite laminated plate under the effect of temperature and combined loading using Lyapunov exponent parameter. Composites. Part. B. 219, (2021) 108926.

[9] S.S. Atteshamuddin, M.G. Yuwaraj. Free vibration analysis of angle-ply laminated composite and soft core sandwich plates. Sand. Struct. Mater. 19 (6) (2017) 679-711.

[10] O. Allam, K. Draiche, A.A. Bousahla, F. Bourada, E.A.A. Bedia. A generalized 4 -unknown refined theory for bending and free vibration analysis of laminated composite and sandwich plates and shells. Comp. Conc. 26 (2) (2020) 185-201.

[11] F. Bourada, A.A. Bousahla, A. Tounsi, E.A.A. Bedia, S.R. Mahmoud, K.H. Benrahou, A. Tounsi. Stability and dynamic analyses of SW-CNT reinforced concrete beam resting on elastic-foundation. Comp. Conc. 25 (6) (2020) 485-495.

[12] N. Belbachir, M. Bourada, K. Draiche, A. Tounsi, S.R. Mahmoud. Thermal flexural analysis of anti-symmetric cross-ply laminated plates using a four variable refined theory. Smart. Struct. Syst. 25 (4) (2020) 409-422.

[13] A.A. Bousahla, F. Bourada, S.R. Mahmoud, A. Tounsi, A. Algarni, E.A.A. Bedia, A. Tounsi. Buckling and dynamic behavior of the simply supported CNT-RC beams using an integral-first shear deformation theory. Comp. Conc. 25 (2) (2020) 155-166.

[14] N. Shabanijafroudi, R. Ganesan. A penalty function based delamination model for postbuckling analysis of composite plates with delamination. Compos. Struct. 261 (2021) 113273.

[15] N. Bendenia, M. Zidour, A.A. Bousahla, F. Bourada, A. Tounsi. Deflections, stresses and free vibration studies of FG-CNT reinforced sandwich plates resting on Pasternak elastic foundation. Comp. Conc. 26 (3) (2020) 213-226.

[16] K. Draiche, A.A. Bousahla, A. Tounsi, A.S. Alwabli, S.R. Mahmoud. Static analysis of laminated reinforced composite plates using a simple first-order shear deformation theory. Comp. Conc. 24 (4) (2019) 369-378.

[17] M. Abualnour, C. Abdelbaki, H. Hebali, A. Kaci, A. Tounsi. Thermomechanical analysis of antisymmetric laminated reinforced composite plates using a new four variable trigonometric refined plate theory. Comp. Conc. 24 (6) (2019) 489-498.

[18] Y. Chen, S.C. Huang, An optimal placement of CLD treatment for vibration suppression of plates, Int. J. Mech. Sci. 44 (2002) 1801–1821.

[19] N. Kumar, S.P. Singh, Experimental study on vibration and damping of curved panel treated with constrained viscoelastic layer, Compos. Struct. 92 (2010) 233–243.

[20] A. Arikoglu, I. Ozkol, Vibration analysis of composite sandwich beams with viscoelastic core by using differential transform method, Compos. Struct. 92 (2010) 3031–3039.

[21] X.Q. Zhou, D.Y Yu, X. Shao, S. Wang, S.Q. Zhang, Simplified-super-element-method for analyzing free flexural vibration characteristics of periodically stiffened-thin-plate filled with viscoelastic damping material, Thin. Wall. Struct. 94 (2015) 234–252.

[22] X. Song, T. Cao, P. Gao, Q. Han, Vibration and damping analysis of cylindrical shell treated with viscoelastic damping materials under elastic boundary conditions via a unified Rayleigh-Ritz method, Int. J. Mech. Sci. 165 (2020) 105158.

[23] Y. Zhang, G. Jin, M. Chen, T. Ye, C. Yang, Y. Yin. Free vibration and damping analysis of porous functionally graded sandwich plates with a viscoelastic core. Compos. Struct. 244 (2020) 112298.

[24] A.M. Zenkour, H.D. El-Shahrany. Quasi-3D theory for the vibration of a magnetostrictive laminated plate on elastic medium with viscoelastic core and faces. Compos. Struct. 257 (2021) 113091.

[25] B. Nayak, S. K. Dwivedy, K. Murthy, Dynamic analysis of magnetorheological elastomer-based sandwich beam with conductive skins under various boundary conditions, J. Sound. Vib. 330 (9) (2011) 1837-1859.

[26] B. Nayak, S. K. Dwivedy, K. S. R. K. Murthy, Dynamic stability of magnetorheological elastomer based adaptive sandwich beam with conductive skins using FEM and the harmonic balance method.

Int. J. Mech. Sci. 77 (2013) 205-216.

[27] B. Nayak, S. K. Dwivedy, K. S. Murthy, Dynamic stability of a rotating sandwich beam with magnetorheological elastomer core, Eur. J. Mech. A-solid. 47 (2014) 143-155.

[28] A.G. Arani, H.K. Arani, Z.K. Maraghi, Vibration analysis of sandwich composite micro-plate under electro-magneto-mechanical loadings, Appl. Math. Model. 40 (23-24) (2016) 10596-10615.

[29] G. Shankar, S.K. Kuar, P.K. Mahato, Vibration analysis and control of smart composite plates with delamination and under hygrothermal environment, Thin. Wall. Struct. 116 (2017) 53-68.

[30] J. Mao, W. Zhang, Linear and nonlinear free and forced vibrations of graphene reinforced piezoelectric composite plate under external voltage excitation, Compos. Struct. 203 (2018) 551-565.

[31] B.A. Selim, Z. Liu, K.M. Liew, Active vibration control of functionally graded graphene nanoplatelets reinforced composite plates integrated with piezoelectric layers, Thin. Wall. Struct. 145 (2019) 106372.

[32] M. Vinyas, K.K. Sunny, D. Harursampath, T. N. Thoi, M.A.R. Loja, Influence of interphase on the multi-physics coupled frequency of three-phase smart magneto-electro-elastic composite plates, Compos. Struct. 226 (2019) 111254.

[33] T. Soleymani, A. G. Arani, On aeroelastic stability of a Piezo-MRE sandwich plate in supersonic airflow, Compos. Struct. 230 (2019) 111532.

[34] H. Bisheh, N. Wu, T. Rabczuk, Free vibration analysis of smart laminated carbon nanotube-reinforced composite cylindrical shells with various boundary conditions in hygrothermal environments, Thin. Wall. Struct. 149 (2020) 106500.

[35] V. Balamurugan, S. Narayanan, Active–passive hybrid damping in beams with enhanced smart constrained layer treatment, Eng. Struct. 24 (2002) 355-363.

[36] J. Plattenburg, J.T. Dreyer, R. Singh, Active and passive damping patches on a thin rectangular plate: A refined analytical model with experimental validation, J. Sound. Vib. 353 (2015) 75-95.

[37] A. Kumar, S. Panda, A. Kumar, V. Narsaria, Performance of a graphite wafer-reinforced viscoelastic composite layer for active-passive damping of plate vibration, Compos. Struct. 186 (2018) 303-314.

[38] R. Rimašauskienė, V. Jūrėnas, M. Radzienski, M. Rimašauskas, W. Ostachowicz, Experimental analysis of active–passive vibration control on thin-walled composite beam, Compos. Struct. 223 (2019) 110975.

[39] A.M. Zenkour, H.D. El-Shahrany. Hygrothermal effect on vibration of magnetostrictive viscoelastic sandwich plates supported by Pasternak's foundations. Thin. Wall. Struct. 157 (2020) 107007.

[40] A.L. Kalamkarov, G.C. Saha, A.V. Georgiades, General micromechanical modeling of smart composite shells with application to smart honeycomb sandwich structures, Compos. Struct. 79 (1) (2007) 18-33.

[41] A.V. Georgiades, K.S. Challagulla, A.L. Kalamkarov, Asymptotic homogenization modeling of smart composite generally orthotropic grid-reinforced shells: part II-applications, Eur. J. Mech. A-solid. 29 (4) (2010) 541-556.

[42] B. Dyniewicz, J. M. Bajkowski, C. I. Bajer, Semi-active control of a sandwich beam partially filled with magnetorheological elastomer, Mech. Syst. Signal Proc. 60-61 (2015) 695-705.

[43] F.S. Eloy, G.F. Gomes, A.C. Ancelotti, S.S. Cunha, A.J.F. Bombard, D.M. Junqueira, Experimental dynamic analysis of composite sandwich beams with magnetorheological honeycomb core, Eng. Struct. 176 (2018) 231-242.

[44] F. Eloy, G. F. Gomes, A. C. Ancelotti, S. S. Cunha, A. J. Bombard, D. M. Junqueira, A numerical-experimental dynamic analysis of composite sandwich beam with magnetorheological elastomer honeycomb core, Compos. Struct. 209 (2019) 242-257.

[45] Z. Zhao, K. Wang, L. Zhang, L.C. Wang, W. L. Song, D. Fang, Stiff reconfigurable polygons for smart connecters and deployable structures, Int. J. Mech. Sci. 161-162 (2019) 105052.

[46] Q. Tao, C. Wang, K. Wang, Z. Xie, H. Tan, Mixed-mode bending of a smart reconfigurable lattice structure with bi-directional corrugated core, Int. J. Mech. Sci. 185 (2020) 105848.

[47] H.T. Thai, T.K. Nguyen, T.P. Vo, J. Lee. Analysis of functionally graded sandwich plates using a new first-order shear deformation theory. Eur. J. Mech. A/Solids. 45 (2014) 211-225.

[48] R. Nebojša, J. Dejan. Thermal buckling of double-layered graphene sheets embedded in an elastic medium with various boundary conditions using a nonlocal new first-order shear deformation theory. Composites. Part B. 97 (2016) 201-215.

[49] H. Li, H. Wu, T. Zhang, B. Wen, Z. Guan, A nonlinear dynamic model of fiber-reinforced composite thin plate with temperature dependence in thermal environment, Composites. Part. B. 162 (2019) 206-218.

[50] H. Li, W. Wang, X. Wang, Q. Han, J. Liu, Z. Qin, J. Xiong, Z. Guan. A nonlinear analytical model of composite plate structure with an MRE function layer considering internal magnetic and temperature fields, Compos. Sci. Tech. 200 (2020) 108445.

[51] L. Chen, X.L. Gong, W. Jiang, J. Yao, H. Deng, W. Li. Investigation on magnetorheological elastomers based on natural rubber. Mater. Sci. 42 (2007) 5483-5492.

[52] H. Li, H. Wu, T. Zhang, B. Wen, Z. Guan. A nonlinear dynamic model of fiber-reinforced composite thin plate with temperature dependence in thermal environment. Composites. Part B. 162 (2019) 206-218.

[53] P. K. Karsh, T. Mukhopadhyay, S. Chakraborty, S. Naskar, S. Dey. A hybrid stochastic sensitivity analysis for low-frequency vibration and low-velocity impact of functionally graded plates. Composites. Part. B. 176 (2019) 107221.

[54] X. Wang, Z. Yuan. Buckling analysis of isotropic skew plates under general in-plane loads by the modified differential quadrature method. Appl. Math. Model. 56 (2018) 83-95.

[55] A. Mahi, E.A.A. Bedia, A. Tounsi, A new hyperbolic shear deformation theory for bending and free vibration analysis of isotropic, functionally graded, sandwich and laminated composite plate, Appl. Math. Model. 39 (9) (2015) 2489-2508.

[56] J. Yang, L. Ma, M.C. Vargas, T. Huang, K.U. Schröder, R. Schmidt, L. Wu, Influence of manufacturing defects on modal properties of composite pyramidal truss-like core sandwich cylindrical panels, Compos. Sci. Tech. 147 (2017) 89-99.

[57] R.K. Behera, S. Akhtar, A. Kumar, Prediction of eigen-frequency of stiffened sandwich composite plates using finite elements, Mater. Today: Proc. 18 (2019) 5292-5299.

[58] J. W. Lee, J. Y. Lee. Contribution rates of normal and shear strain energies to the natural frequencies of functionally graded shear deformation beams. Composites. Part. B. 159 (2019) 86-104.

[59] R.K. Behera, S.S. Patro, N. Sharma, K.K. Joshi, Eigen-frequency analysis of stiffened composite plates using finite elements, Mater. Today: Proc. 5 (2018) 20152-20159.

[60] C.C. Chao, J.C. Lee, Vibration of eccentrically stiffened laminates, Compos. Mater. 14 (1980) 233-244.

[61] L. Dai, Y. Chen, Y. Wang, Y. Lin. Experimental and numerical analysis on vibration of plate with multiple cutouts based on primitive cell plate with double cutouts, Int. J. Mech. Sci. 183 (2020) 105758.

[62] T.P. Kumar, S.K. Dwivedy, Dynamic analysis of MRE embedded sandwich plate using FEM, Proc. Eng. 144 (2016) 721-728.

[63] R.B. Vemuluri, V. Rajamohan, A.B. Arumugam, Dynamic characterization of tapered laminated composite sandwich plates partially treated with magnetorheological elastomer, J. Sandwich. Struct. Mater. 0 (2016) 1-43.

[64] H. Li, Y Niu, Z. Li, Z. Xu, Q. Han, Modeling of amplitude-dependent damping characteristics of fiber reinforced composite thin plate, Appl. Math. Model. 80 (2020) 394-407.

[65] T.Y. Zhao, Y. Ma, H.Y. Zhang, H.G. Pan, Y. Cai, Free vibration analysis of a rotating graphene nanoplatelet reinforced pre-twist blade-disk assembly with a setting angle, Appl. Math. Model. 93 (2021) 578-596.

[66] H. Li, H. Lv, H. Sun, Z. Qin, J. Xiong, Q. Han, J. Liu, X. Wang, Nonlinear Vibrations of Fiber-reinforced Composite Cylindrical Shells with Bolt Loosening Boundary Conditions, J. Sound. Vib. 0 (2021) 115935.

[67] N.K. Mandal, R.A. Rahman, M.S. Leong, Experimental study on loss factor for corrugated plates by bandwidth method, Ocean. Eng. 31 (10) (2004) 1313-1323.

Appendix A

Based on the energy method, the total kinetic energy T_s^* and potential energy U_s^* for GFUs can be expressed as

$$T_s^* = \sum_{i=1}^{n_u} \left(\frac{1}{2} \dot{\boldsymbol{\delta}}_i^{gf\mathrm{T}} \boldsymbol{M}_i^{gf} \dot{\boldsymbol{\delta}}_i^{gf} + \frac{1}{2} \dot{\boldsymbol{\delta}}_i^{p\mathrm{T}} \boldsymbol{M}_i^{p} \dot{\boldsymbol{\delta}}_i^{p} + \dot{\boldsymbol{\delta}}_i^{c\mathrm{T}} \boldsymbol{M}_i^{c} \dot{\boldsymbol{\delta}}_i^{c} + \frac{1}{2} \dot{\boldsymbol{\delta}}_i^{v\mathrm{T}} \boldsymbol{M}_i^{v} \dot{\boldsymbol{\delta}}_i^{v} \right) \tag{A.1}$$

$$U_s^* = \sum_{i=1}^{n_u} \left(\frac{1}{2} \boldsymbol{\delta}_i^{gf\mathrm{T}} \boldsymbol{K}_i^{gf} \boldsymbol{\delta}_i^{gf} + \frac{1}{2} \boldsymbol{\delta}_i^{p\mathrm{T}} \boldsymbol{K}_i^{p} \boldsymbol{\delta}_i^{p} + \boldsymbol{\delta}_i^{c\mathrm{T}} \boldsymbol{K}_i^{c} \boldsymbol{\delta}_i^{c} + \frac{1}{2} \boldsymbol{\delta}_i^{v\mathrm{T}} \boldsymbol{K}_i^{v} \boldsymbol{\delta}_i^{v} \right) \tag{A.2}$$

Appendix B

The modal functions $P_m(\alpha)$ and $P_n(\beta)$ adopted in Eq. (24) along the x and y directions of the CFRP-GFB-GFU plate are given as

$$\begin{gathered}
P_1(\alpha) = \phi(\alpha),\ P_1(\beta) = \varphi(\beta),\ P_2(\zeta) = (\zeta - B_2) P_1(\zeta),\ P_b(\zeta) = (\zeta - B_b) P_{b-1}(\zeta) - C_b P_{b-2}(\zeta), \\
B_k = \frac{\int_0^1 \left[P_{k-1}(\zeta) \right]^2 \zeta d\zeta}{\int_0^1 \left[P_{k-1}(\zeta) \right]^2 d\zeta},\ C_k = \frac{\int_0^1 P_{k-1}(\zeta) P_{k-2}(\zeta) \zeta d\zeta}{\int_0^1 \left[P_{k-2}(\zeta) \right]^2 d\zeta} \\
\phi(\alpha) = \alpha^p (1-\alpha)^q,\ \varphi(\beta) = \beta^r (1-\beta)^s,\ \zeta = \alpha, \beta;\quad \alpha = x/a,\quad \beta = y/b;\quad b > 2
\end{gathered} \tag{B.1}$$

Here, for the free, simple and fixed boundary conditions, the values of p, q, r, s are can be set as 0, 1, 2, respectively.

Appendix C

To solve the damping property, the strain energy U and the dissipation energy ΔU are expressed as

$$\begin{aligned}
U = \mathrm{R}(U^*) = \mathrm{R}\Big(& \sum_{i=1}^{n_u} \left(\frac{1}{2} \boldsymbol{\delta}_i^{gf\mathrm{T}} \boldsymbol{K}_i^{gf} \boldsymbol{\delta}_i^{gf} + \frac{1}{2} \boldsymbol{\delta}_i^{p\mathrm{T}} \boldsymbol{K}_i^{p} \boldsymbol{\delta}_i^{p} + \boldsymbol{\delta}_i^{c\mathrm{T}} \boldsymbol{K}_i^{c} \boldsymbol{\delta}_i^{c} + \frac{1}{2} \boldsymbol{\delta}_i^{v\mathrm{T}} \boldsymbol{K}_i^{v} \boldsymbol{\delta}_i^{v} \right) \\
& + \sum_{i_x=1}^{n_x} \frac{1}{2} \boldsymbol{\delta}_{i_x}^{gb\mathrm{T}} \boldsymbol{K}_{i_x}^{gb} \boldsymbol{\delta}_{i_x}^{gb} + \sum_{i_y=1}^{n_y} \frac{1}{2} \boldsymbol{\delta}_{i_y}^{gb\mathrm{T}} \boldsymbol{K}_{i_y}^{gb} \boldsymbol{\delta}_{i_y}^{gb} + \boldsymbol{\delta}^{f\mathrm{T}} \boldsymbol{K}^{f} \boldsymbol{\delta}^{f} \Big)
\end{aligned} \tag{C.1}$$

$$\begin{aligned}
\Delta U = \mathrm{I}(U^*) = \mathrm{I}\Big(& \sum_{i=1}^{n_u} \left(\frac{1}{2} \boldsymbol{\delta}_i^{gf\mathrm{T}} \boldsymbol{K}_i^{gf} \boldsymbol{\delta}_i^{gf} + \frac{1}{2} \boldsymbol{\delta}_i^{p\mathrm{T}} \boldsymbol{K}_i^{p} \boldsymbol{\delta}_i^{p} + \boldsymbol{\delta}_i^{c\mathrm{T}} \boldsymbol{K}_i^{c} \boldsymbol{\delta}_i^{c} + \frac{1}{2} \boldsymbol{\delta}_i^{v\mathrm{T}} \boldsymbol{K}_i^{v} \boldsymbol{\delta}_i^{v} \right) \\
& + \sum_{i_x=1}^{n_x} \frac{1}{2} \boldsymbol{\delta}_{i_x}^{gb\mathrm{T}} \boldsymbol{K}_{i_x}^{gb} \boldsymbol{\delta}_{i_x}^{gb} + \sum_{i_y=1}^{n_y} \frac{1}{2} \boldsymbol{\delta}_{i_y}^{gb\mathrm{T}} \boldsymbol{K}_{i_y}^{gb} \boldsymbol{\delta}_{i_y}^{gb} + \boldsymbol{\delta}^{f\mathrm{T}} \boldsymbol{K}^{f} \boldsymbol{\delta}^{f} \Big)
\end{aligned} \tag{C.2}$$

Appendix D

The magnetic field dependent shear modulus and loss factor values of MRE material [63] are shown as follows.

$$G_{v12} = 2.7006 + 2.43B + 38.778B^2 - 93.422B^3 + 71.797B^4 - 9.1077B^5 - 6.9395B^6 \quad \text{(D.1)}$$

$$\eta_{v12} = 0.228 + 0.1526B + 2.3522B^2 - 12.185B^3 + 22.148B^4 - 17.787B^5 - 5.3485B^6 \quad \text{(D.1)}$$

Highlights

■ An integrated material and structure design approach is proposed for fabrication of a multifunctional grille composite sandwich plate

■ A dynamic model of the multifunctional grille composite sandwich plates is proposed to predict the free vibration and damping characteristics.

■ Numerical and experimental validation are conducted to prove the effectiveness of the present model

■ Parametric studies are performed to improve the structural vibration suppression capacity and stiffness performance

Declaration of Conflicting interests

The authors declared no potential conflicts of interest with respect to the research, authorship, and/or publication of this article.

Sincerely,

Jian Xiong

Address: Center for Composite Materials and Structures, Harbin Institute of Technology, Harbin 150001, China

E-mail: jx@hit.edu.cn

Tel: +86 0451 86402376

Fax: +86 0451 86402376